

**DEVELOPMENT OF A DISPENSING BASED ADDITIVE MANUFACTURING
TECHNIQUE FOR THE CREATION OF ALGINATE BONE SCAFFOLDS**

by

Varun Jacob-John

B.A.Sc., University of Waterloo, 2016

A THESIS SUBMITTED IN PARTIAL FULFILLMENT OF
THE REQUIREMENTS FOR THE DEGREE OF

MASTER OF APPLIED SCIENCE

in

THE FACULTY OF GRADUATE AND POSTDOCTORAL STUDIES
(Mechanical Engineering)

THE UNIVERSITY OF BRITISH COLUMBIA

(Vancouver)

April 2019

© Varun Jacob-John, 2019

The following individuals certify that they have read, and recommend to the Faculty of Graduate and Postdoctoral Studies for acceptance, a thesis/dissertation entitled:

Development of a Dispensing Based Additive Manufacturing Technique for the Creation of Alginate Bone Scaffolds

submitted by Varun Jacob-John in partial fulfillment of the requirements for

the degree of Master of Applied Science

in Mechanical Engineering

Examining Committee:

Dr. Yusuf Altintas

Supervisor

Dr. Rizhi Wang

Co-supervisor

Dr. Ryozo Nagamune

Additional Examiner

Dr. Xiaoliang Jin

Additional Examiner

Abstract

Bone scaffolds are used to treat large bone defects. There are noted advantages for moving away from the standard of using human bone to create these scaffolds, and instead making them out of synthetic biomaterials. Dispensing Based Additive Manufacturing (DBAM) provides a method for creating these synthetic bone scaffolds using a biomaterial called alginate. This thesis outlines a method to create synthetic bone scaffolds from alginate using DBAM.

First an ink was developed to be used with DBAM, consisting of sodium alginate, calcium carbonate and a photoacid generator. This ink was able to react when exposed to Ultraviolet (UV) light to partially gel, as required between layers in the DBAM process. Studies were conducted to find the ideal concentrations of the components of the ink. The gelation in between layers was modelled to determine the ideal layer thickness, UV lamp intensity and exposure time that would lead to the ideal mechanical properties for a partially gelled layer.

The dispensing process was modelled to determine the height and width of an extruded line based on the applied pressure, needle diameter, and needle length. This model has been used to determine the ideal pressure to achieve a desired layer height. A commercial software was used to convert three-dimensional commanded shapes to two-dimensional layer toolpaths. Advanced trajectory techniques have been used to generate a time-based trajectory from these toolpaths that would minimize traversal time, while staying within the velocity, acceleration and jerk limits of the in-house developed Computer Numerical Controlled (CNC) machine. The dispensing was synchronized with the tangential speed of the machine to keep dispensed width constant.

Sample parts have been manufactured using the developed DBAM process, with an improved dimensional accuracy and mechanical stiffness in comparison to results reported in literature.

Lay Summary

Bone scaffolds are structures used to help the body heal from large breaks in bone. While they are normally made from human bone taken from elsewhere, there are potential benefits in making these parts out of synthetic biomaterials. One way of producing synthetic bone scaffolds is dispensing based additive manufacturing (DBAM), a process that builds a part layer-by-layer by dispensing a liquid ink in a given shape for a layer, which is then made solid, and built on top of. This thesis develops a method to create synthetic bone scaffolds out of a biomaterial called alginate, via DBAM. This includes work in determining how to create the correct ink, what are the best inputs to get the desired outputs, and how best to move the machine.

Preface

I was the lead investigator for the work presented in Chapters 3, 4 and 5. I created the relevant models, planned the experiments and completed analysis of the results. Dr. Yusuf Altintas was the chief supervisor and Dr. Rizhi Wang was the co-supervisor for the work.

Table of Contents

Abstract.....	iii
Lay Summary	v
Preface.....	vi
Table of Contents	vii
List of Tables	ix
List of Figures.....	x
List of Symbols	xii
Acknowledgements	xv
Chapter 1: Introduction	1
Chapter 2: Literature Review.....	5
2.1 Bone Scaffolds	5
2.2 Dispensing Based Additive Manufacturing	6
2.3 Alginate for Biomedical Applications	7
2.4 Summary	8
Chapter 3: Development and Modelling of Alginate Ink	9
3.1 Development of Alginate Ink.....	9
3.1.1 Ionic Crosslinking of Alginate with Calcium	9
3.1.2 Crosslinking of Alginate with UV Light	11
3.1.3 Experimental Creation of Ink.....	13
3.1.4 Concentration Study.....	13
3.2 Modelling of Mid-layer Gelation.....	16
3.2.1 Formation of Mechanical Model	18

vii

3.2.2	Experimental Model Parameter Identification	20
3.2.3	Experimental Results	24
Chapter 4: Modelling and Control of Dispensing Step		29
4.1	Modelling of Dispensing Process	29
4.1.1	Derivation of Flow Rate Model	30
4.1.2	Calculating Model Parameters via Rheological Measurement	32
4.1.3	Experimental Validation of Flow Rate Model.....	36
4.1.4	Modelling of Deposited Height and Width.....	38
4.2	Trajectory Generation	40
4.2.1	Slicing of 3D Models	41
4.2.2	Creation of 2D Toolpath	43
4.2.3	Feedrate Optimization.....	46
4.2.4	Synchronized Dispensing.....	47
4.2.5	Experimental Validation of Trajectory Generation Techniques	49
Chapter 5: Evaluation of Experimentally Manufactured Parts.....		54
5.1	Input Parameters and Settings Used	54
5.2	Observations of Manufactured Part	56
5.3	Evaluation of Mechanical Properties	59
Chapter 6: Conclusion.....		61
6.1	Future Work	62
Bibliography		64

List of Tables

Table 3.1: Summary of concentrations of different inks used for concentration study.....	15
Table 3.2: Pictures of 15mm circles extruded with the different inks at different pressure levels.	15
Table 3.3: Measurement of mass loss for layer after UV exposure.....	27
Table 4.1: Comparison between original straight-line G-code path to spline and feedrate optimized path.....	52
Table 5.1: Summary of Input parameters used for part manufacturing.....	56
Table 5.2: Summary of diameter and height measure for manufactured parts	58
Table 5.3: Measured compressive stiffness of manufactured parts.	59
Table 5.4: Report Compressive Stiffness of Alginate hydrogel from literature	60

List of Figures

Figure 1.1: Overview of Dispensing Based Additive Manufacturing	2
Figure 1.2: Outline of thesis method based on dispensing based additive manufacturing process	4
Figure 3.1 The effect of crosslinking of alginate: (a) sodium alginate floating independently in solution; (b) calcium alginate linking together to create hydrogel	10
Figure 3.2: Representation of the Kelvin-Voigt (left) and Maxwell (right) models for viscoelasticity.....	18
Figure 3.3: The Burger model for viscoelasticity, including applied stress σ and resulting strain response ϵ	18
Figure 3.4: Experimental setup for Burger model parameter identification: (a) represents the general components; (b) represents the position at $t = 0$; (c) represents the position at the end of the experiment.....	21
Figure 3.5 Image of Uvitron IntelliRay 600 UV Flood Lamp[19]	21
Figure 3.6: Expected response of a Burger model material to a constant applied stress.....	23
Figure 3.7: Identified Burger Model Parameters for single layer of thickness 0.55mm, where exposure time and lamp intensity are varied.....	24
Figure 3.8: Identified Burger Model Parameters for single layer of thickness 0.90mm, where exposure time and lamp intensity are varied.....	25
Figure 3.9: Pictures of 0.55mm layer after 75% intensity exposure of increasing times.	27
Figure 4.1: Illustration of inputs and outputs of the dispensing model.	30
Figure 4.2: Measurement of viscosity of ink at different shear rates at different frequencies	33
Figure 4.3: Fit of the cross model to the measurement data.	35
Figure 4.4 Summary of Techcon TS350 Digital Fluid Dispenser [22].....	36

Figure 4.5: Comparison of predicted flow rate using the calculated parameters, predicted flow rate using experimentally fit parameters, and the experimentally measured flow rates.	37
Figure 4.6: Representation of the circle section cross sectional area.	38
Figure 4.7 Overview of trajectory generation method in this chapter.	41
Figure 4.8 Input of a cube with side length 20mm into Slic3r.	42
Figure 4.9: Layer with infill created by Slic3r for the simple cube shape.	43
Figure 4.10: Interpolation of pass-through points to create spline. Blue x's represent the original points from G-code, and red circles represent the new interpolated points.	45
Figure 4.11: Spline fitting: original path from the G-code is seen in blue, and the new fitted spline is in red.	45
Figure 4.12: For spline toolpath on the left, the calculated feedrate spline on the right. Dips in the feedrate spline correspond to sharp turns in toolpath.	47
Figure 4.13 Image of 3-axis CNC machine	49
Figure 4.14 Bode Plot showing Matched Motion Axis Dynamics of the three axes	50
Figure 4.15: Comparison of tracking error in X and Y for the original straight-line G-code path to spline and feedrate optimized path	51
Figure 4.16: Evaluation of the effect of the PWM-based synchronized dispensing: on the left is constant dispensing, and on the right is when synchronized dispensing is used.	52
Figure 5.1: Simple cylinder shape to be manufactured to evaluate the DBAM process.	54
Figure 5.2: Sample layer generated by Slic3r for parts: (a) 40%, (b) 60%, and (c) 80% dense... ..	55
Figure 5.3: Preview of the full shapes in Slic3r: (a) 40%, (b) 60%, and (c) 80% dense.	55
Figure 5.4: Pictures of manufactured parts.	57

List of Symbols

Na^+	Sodium Ion
Ca^{2+}	Calcium Ion
H^+	Hydrogel Ion
$CaCl_2$	Calcium chloride
PAG	Photoacid Generator
$CaCO_3$	Calcium carbonate
E_K	Kelvin-Voigt elasticity in Burger Model
η_K	Kelvin-Voigt viscosity in Burger Model
E_M	Maxwell elasticity in Burger Model
η_M	Maxwell viscosity in Burger Model
σ	Applied Stress
ε	Strain
ε_{E_M}	Strain in Maxwell Elasticity
ε_{η_M}	Strain in Maxwell Viscosity
ε_K	Strain in parallel Kelvin-Voigt elements
σ_0	Constant Applied Stress
t	Time
g	Acceleration due to Gravity
m	Mass of Object from Burger Model Experiment
A	Cross-Sectional Area of Object from Burger Model Experiment
$T(t)$	Layer Thickness as a Function of Time from Burger Model Experiment

T_0	Original Layer Thickness
C_1, C_2, C_3, C_4	Constant Coefficients used in Burger Model Experiment
P	Dispenser Applied Pressure
v	Machine movement velocity
L	Dispenser Needle Length
D	Dispenser Needle Diameter
h	Height of a Dispensed Line
w	Width of a Dispensed Line
Q	Volumetric Flow Rate from Syringe
n	Power Law Index from Flow Rate Model
η_0	Specific Viscosity
$\dot{\gamma}_0$	Specific Shear Rate
a, b	Constant Parameters Used for Dispensing Model
η	Viscosity of Ink
$\dot{\gamma}$	Shear Rate
K	Consistency Coefficient from Power Law Model
n_p	Power Law Index from Power Law Model
η_∞	Infinite Shear Viscosity from Cross Fluid Model
η_{0c}	Zero Shear Viscosity from Cross Fluid Model
m_c	Cross Rate Constant from Cross Fluid Model
C	Cross Time Constant from Cross Fluid Model
m_d	Dispensed Mass from Flow Rate Model Experiment

t_d	Dispense Time from Flow Rate Model Experiment
ρ	Density of Ink
A_d	Cross Sectional Area of a Dispensed Line
R	Radius of Circle from which Circle Section of A_d is taken
θ	Contact Angle
u	Spline parameter
$P(u)$	Toolpath Position spline, as a function of spline parameter u
s	Path displacement along the toolpath spline
PWM	Pulse Width Modulation
d	Duty Cycle for Dispenser Pulse Width Modulation

Acknowledgements

I am extremely grateful to my supervisor Dr. Yusuf Altintas for his incredible support and guidance throughout my graduate studies. He always made sure I had everything I need, and through him I have gotten unparalleled insight into both research and manufacturing engineering. I am very appreciative of the opportunity to work with him and to have received his mentorship.

I would also like to thank my co-supervisor, Dr. Rizhi Wang, who provided invaluable guidance for many of the tougher challenges in my research. The insight he provided into biomaterials and the biomedical field was incredibly valuable, and his positivity was always encouraging.

I would also like to thank Harun Arkaz for his assistance in the theoretical materials work and in designing the experiments, and for always making time to help me. I would like to thank Hale Oguzlu-Baldelli and Jessica Zhang for their help in some of the experiments conducted.

To my friends in the Manufacturing Automation Laboratory, you made every day more fun. The research support, as well as the emotional support was such an amazing boon during throughout. I will always remember our great daily conversations and discussions.

To my friends in the Biomaterials group, your endless positivity and willingness to help in any situation was extremely heartening.

Finally, I need to thank my family, who always encouraged me to pursue excellence in everything I do, and get the best education I can. My brother, my parents and my grandparents were always there as support whenever I needed it.

This research is supported by the National Sciences and Engineering Research Council of Canada CANRIMT2 Strategic Research Network Grant (NETGP 479639-15) in machining.

Chapter 1: Introduction

In a human body, long bone defects may be caused by trauma or abnormal skeletal development, or due to surgical resection of diseased or cancerous bone, resulting in large sections of bone missing. While the human body is very good at regrowing bone, especially in younger people, large defects lack a template or guidance for this regrowth, preventing the bone from healing properly, and potentially resulting in irregular growth. The current standard of care for treatment of these long bone defects are bone scaffolds: bone-like structures that are implemented in the place where the bone is missing, giving short term mechanical support in the broken area and providing the necessary guidance to encourage growth of the bone along the scaffold. As the bone regrows, it will replace the bone scaffold, and the temporary scaffold material will be absorbed by the body when it is no longer needed.

Currently, bone scaffolds are mostly made from human bone, taken from elsewhere in the same patient's body, known as an autograft, or from another body, known as an allograft. However, each of these possible sources have associated problems: autografts can result in complications such as pain, infection or morbidity at the site the bone is harvested from, and allografts have possible negative complications like disease transfer or immune-rejection reactions.

Synthetic scaffolds created from other biomaterials instead of human bone, is currently an area of active research. Synthetic scaffolds would avoid issues from the donor site of an autograft, or with potential rejection of an allograft. In addition, a synthetically created scaffold has other potential benefits, such as a high degree of customizability in shape, porosity, mechanical properties, and potential additives. To be viable, these synthetic bone scaffolds need to be able to

reflect the properties of real bone: it must be similarly porous, and have a similar mechanical strength. In addition, the synthetic material must be biocompatible, so that it can exist in the body without causing any issues with the patient, and biodegradable, so that it can be absorbed by the body after it has completed its function. These scaffolds can be made of many different materials, like ceramic, polymer, or composites.

Synthetic bone scaffolds can be created through a variety of methods. One way is through additive manufacturing: the building up of a part layer by layer. Additive manufacturing offers significant advantages over other methods as it allows for easy creation of one-off parts with control over material, shape and mechanical properties of the produced part. One particular technique of additive manufacturing that can be applied to bone scaffolds is known as Dispensing Based Additive Manufacturing (DBAM), an overview of which is seen in Figure 1.1. A liquid solution, known as an ink is prepared and placed into a syringe. Next, the ink is dispensed from the syringe into a shape that corresponds to a given layer of the final part. After this, the dispensed layer of ink is made into a more solid three-dimensional (3D) shape after being dispensed. The dispensing and 3D formation are repeated for multiple layers, until the full part has been produced.

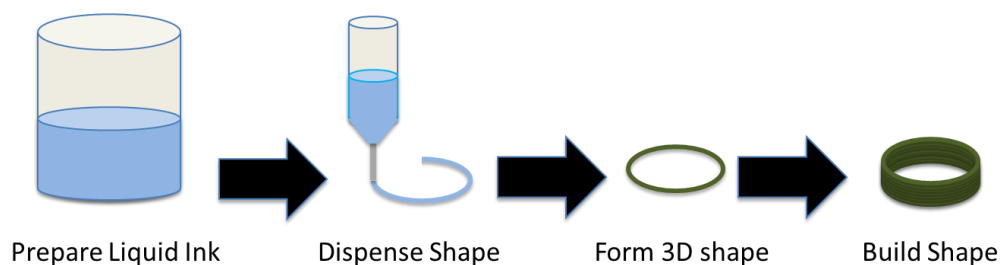


Figure 1.1: Overview of Dispensing Based Additive Manufacturing

DBAM boasts some notable benefits over both conventional synthetic bone scaffold creation methods and other methods of additive manufacturing. Not only is it easy to implement, it is very versatile, capable of manufacturing with many different material types. DBAM requires only three-dimensional movement of a syringe with respect to a base, and a device to dispense liquid from a syringe. These minimal requirements allows for DBAM to be easily created from a simple setup without the need of complex post-processing steps or complex machines. In addition, DBAM requires an ink that is initially liquid and can later be converted into a solid after dispensing, leading to a flexibility that provides many options for ink materials. On top of the base material, additives can also be incorporated into the ink to change material properties.

With the available versatility of DBAM, there are many potential materials which can be used for ink suitable for creating bone scaffolds. Biopolymer materials are easy to use, compatible with the body, and typically require no post-processing when working. Of these biopolymers, a commonly cited polymer for bone scaffold is alginate, a material that is derived from brown sea weed. Alginate is easy to obtain and use in a solution, is biocompatible, and is naturally porous, making it an ideal material for bone scaffolds. Alginate is readily obtainable as a liquid solution, but can be turned into a solid shape, via a process called gelation.

In this thesis, a method which employs DBAM to create bone scaffolds out of alginate is proposed. To achieve this objective, the following goals need to be accomplished: developing an alginate based ink to be compatible with the DBAM process, developing a model for the gelation of the ink between layers, developing a model for dispensing, and developing advanced

trajectory generation techniques to create time-based commands for machine movement. The application of these steps to the DBAM process can be seen in Figure 1.2.

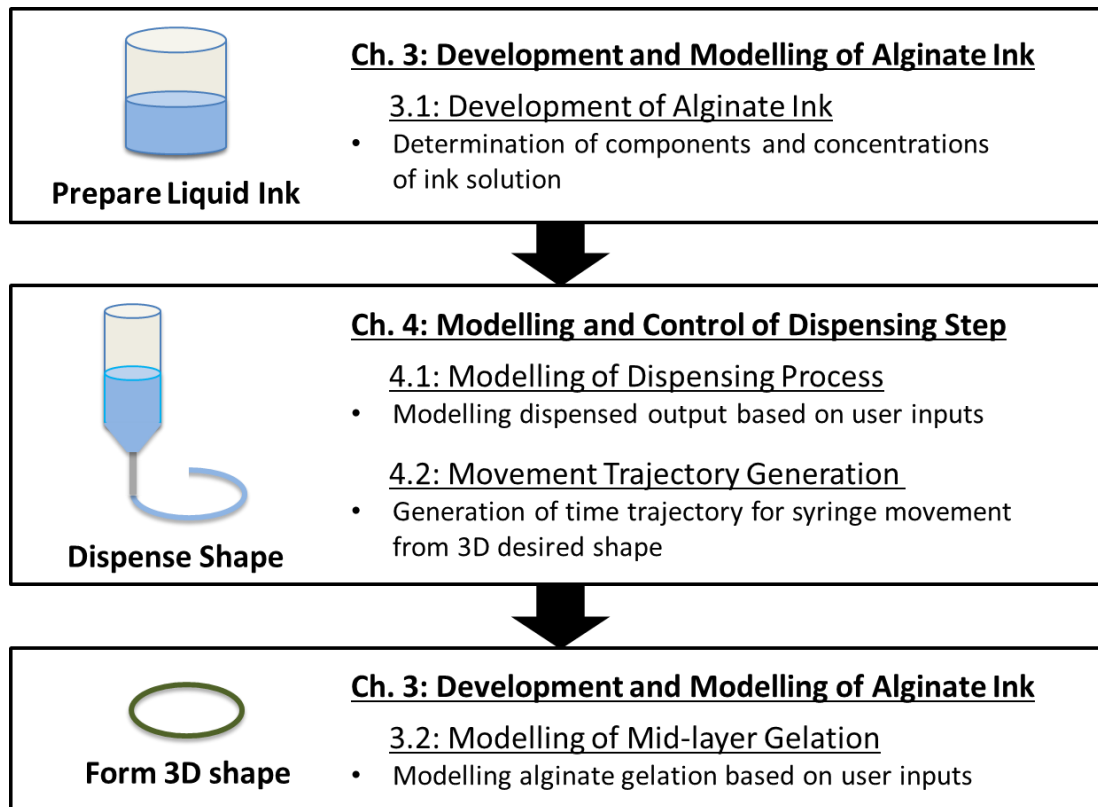


Figure 1.2: Outline of thesis method based on dispensing based additive manufacturing process

The rest of the thesis is structured as followed: Chapter 2: presents a review of work done in bone scaffolds, dispensing based additive manufacturing, and alginate. Chapter 3: presents the development of the specific ink to be used, and a model for mid-layer gelation. Chapter 4: presents development of the models for the dispensing, and the adapted trajectory generation techniques. Chapter 5: presents experimentally manufactured parts made through this process and evaluates dimensional accuracy and mechanical strength. Chapter 6: concludes the thesis with some final comments, and discussion of possible extensions and future research.

Chapter 2: Literature Review

The production of synthetic bone scaffolds is a rich field of research, due to the promising benefits and reduced risk compared to autografts and allografts. As such there has been a recent influx of work in the field reviewing materials and production techniques to create synthetic scaffolds. In order to inform the efforts to create alginate bone scaffolds with DBAM, this chapter presents past research conducted in bone scaffolds, DBAM and alginate as a material.

2.1 Bone Scaffolds

Firstly, the work done in bone scaffolds is investigated. Verrier et al. [1] looked at the difficulties of the body to heal large bone defects, and how bone scaffolds can be an effective treatment option to assist with healing. Kurien et al. [2] looked at the clinical potential of synthetic bone scaffolds, their benefits over autografts and allografts and how synthetic bone scaffolds can be implemented in a way that takes advantage of their benefits. Stevens [3] reviewed biomaterials which can be used for bone tissue engineering, including bone scaffolds. The work recognizes the need for scaffolds to promote differentiation of cells after implanting, support bone growth, integrate into the surround bone, and then eventually be reabsorbed and replaced over time. Common types of materials that can be used for bone scaffolds were identified: bioactive ceramics, bioactive glasses, polymers, and composites of these materials. Bose et al. [4] reviewed multiple ways bone scaffolds can be produced via additive manufacturing, outlining work that has created bone scaffolds using 3D printing, laser-assisted bioprinting, selective laser sintering, stereolithography, fused deposition modelling and dispensing based additive manufacturing. For each of these different methods, the compatible different materials were identified and could be used to create a viable bone scaffold.

2.2 Dispensing Based Additive Manufacturing

There has been some work in the development of dispensing based additive manufacturing to create bone scaffolds. Throughout literature, there are many different names for the process that is called “dispensing based additive manufacturing” in this thesis. The process is very versatile, being able to make parts with many different materials. For example, Hung et al. [5] detailed “dispensing printing” to create parts out of polycaprolactone (PCL). Xiong et al. [6] presented “low-temperature deposition” to create parts of polylactic acid (PLA). Franco et al. [7] presented “direct write assembly” to create parts of calcium phosphate ceramic. Geng et al. [8] showed “direct writing” of chitosan, a biopolymer derived from shrimp shells. All of these works feature the creation of an ink from their respective materials, which is extruded in liquid form layer-by-layer and made solid after extrusion. Most of this work focuses on the material being used, and the derivation and creation of the ink. Work has also been done looking closer at the dispensing process. DBAM works by having a syringe with the ink inside, mounted to a three-axis machine. For each layer, the syringe is moved in the x and y directions relative to a base, on which it can dispense a layer. After this liquid layer has been made solid, the syringe can be moved up slightly in the z direction to dispense another layer on top. Li et al. [9] review “dispensing-based rapid prototyping” techniques, looking at different ways the ink can be extruded, and different possible mechanisms behind the conversion of the ink to three-dimensional (3D) form. The work goes on to model the flow rates seen in the extrusion process, and control of other properties like porosity. Khalil and Sun [10] looked at the extrusion of ink, and established models for the extrusion flow rates for an ink that was a non-Newtonian fluid.

2.3 Alginate for Biomedical Applications

While there are many materials that can be used to create bone scaffolds, one very common material seen in literature is alginate. Lee and Mooney [11] investigated the properties of alginate, and how it could be used in biomedical applications like bone scaffolds. Alginate, as a natural polymer, is extracted from brown seaweed and can be made solid through gelation into a hydrogel via ionic crosslinking in the presence of calcium ions. Ionic crosslinking can be practically achieved by exposing alginate to a solution rich in calcium ions, like a calcium chloride solution. Hydrogels are cross-linked networks made of a hydrophilic polymer, like alginate, featuring a high water content. Venkatesan et al. [12] reviewed the properties of alginate scaffolds, including their excellent biocompatibility, biodegradability, pore size control, and inexpensiveness, and the potential of alginate bone scaffolds as a delivery vehicle for stem cells or drugs. Kuo and Ma [13] looked at the mechanical properties of alginate scaffolds, and into the crosslinking process, including swelling that may occur. Tabriz et al. [14] looked at bioprinting of alginate scaffolds laden with cells. This process, which is very similar to dispensing based additive manufacturing, allows alginate scaffolds to be embedded with active cells. The alginate was deposited, and then lowered into a bath of cell culture medium containing calcium chloride, to activate gelation after a layer is deposited.

Other techniques that can be used to induce gelation were also investigated. In their work, Javvaji et al. [15] determined a way to activate ionic gelation using Ultraviolet (UV) light, by preparing a solution of alginate mixed with insoluble calcium carbonate and a photoacid generator. Upon exposure to UV light, the photoacid generator will release acid which will allow the calcium carbonate to dissolve, releasing calcium ions that will induce gelation. This process

will be further described in Chapter 4. Javvaji's work was later expanded by Higham et al. [16], who conducted experiments to see the change in the induced gelation based on changes in solution concentrations, light intensity and exposure duration. However, both Javvaji's and Higham's work applied to large volumes of alginate solution being gelled together, in a way that is incompatible with the small volume of a single layer in dispensing based additive manufacturing. Valentin et al. [17] looked into using this UV based technique in stereolithography, another form of additive manufacturing, which operates by having a large volume of the alginate solution that is selective gelled by UV light for a given layer, and slowly lifted out of the solution. As a result, the specific mechanics of this technique will be quite different from the dispensing based additive manufacturing.

2.4 Summary

Through all the literature, a lot of work has been done in determining the materials to be used for bone scaffolds and in DBAM. The desirable versatility of DBAM and suitability of alginate for bone scaffolds have been well established. However, not a lot of work has been found that focuses on the nature of the manufacturing process, and into modelling components of that process. Also, the UV activated gelation has not been applied to dispensing based additive manufacturing, where it can be a good way to achieve the necessary gelation.

This thesis proposes the production of alginate bone scaffolds via dispensing based additive manufacturing. Using an established material and ink combination, the focus is on modelling the different parts of the process in order to better control the manufacturing of an ideal final part.

Chapter 3: Development and Modelling of Alginate Ink

A main component for the dispensing based additive manufacturing is the ink, which is initially in a liquid form, and can be made into a more solid form after it has been extruded. Section 3.1 outlines the development of an alginate based ink that can be used for making bone scaffold via DBAM. Section 3.2 outlines the model developed for the mid-layer gelation used to convert from the liquid to solid form.

3.1 Development of Alginate Ink

The ink to be used with DBAM needs to be a solution that is able to become more solid after being dispensed. Section 3.1.1 outlines the commonly used ionic crosslinking process that is used to create hydrogels from alginate. Section 3.1.2 outlines a modified version of this crosslinking process that can be activated with UV light, and the additional components necessary in the ink. Section 3.1.3 outlines the materials used, and the procedure to mix the ink. Lastly, section 3.1.4 outlines a study conducted to determine the ideal concentrations for the components in the ink.

3.1.1 Ionic Crosslinking of Alginate with Calcium

While derived from seaweed, alginate is typically available commercially as sodium alginate powder, which can be dissolved in water to create a liquid solution. In this form, alginate can be represented as short chains attached to sodium ions (Na^+), as illustrated in Figure 3.1a. When sodium alginate in solution comes in contact with calcium ions (Ca^{2+}), the calcium ions displace the sodium ions. However, due to their charge, one calcium ion attaches to two alginate chains, allowing the alginate chains to connect via calcium ions to create more cohesive structures, as

seen in Figure 3.1b, resulting in the formation of the final desired hydrogel. Within the context of DBAM, the goal is to take advantage of this gelation to convert liquid sodium alginate solution to a solid calcium alginate hydrogel after it has been dispensed by somehow exposing extruded sodium alginate ink to calcium ions. The reaction is summarized in Equation (3.1).

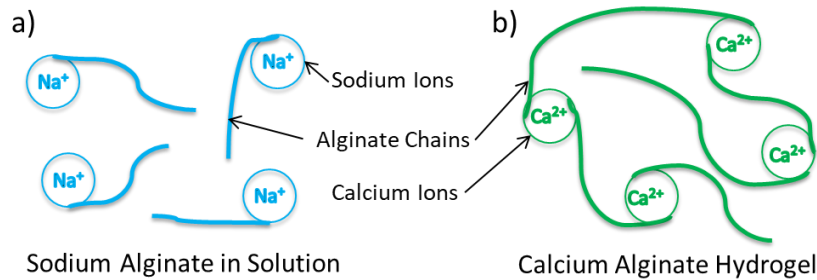
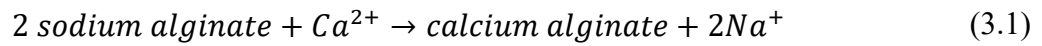


Figure 3.1 The effect of crosslinking of alginate: (a) sodium alginate floating independently in solution; (b) calcium alginate linking together to create hydrogel

Difficulty arises in determining how to practically accomplish this ionic crosslinking for DBAM, as it needs to be done after each layer has been dispensed. The simplest way is to expose the sodium alginate to a solution rich in calcium ions, like a calcium chloride (CaCl_2) solution. When the sodium alginate ink is exposed to calcium chloride solution, the gelation happens immediately. Due to the immediate gelation, sodium alginate ink cannot be dispensed directly into calcium chloride solution at the base, as it results in bits of hydrogel floating around in the solution, instead of joining together to create the intended shape. If the solution is poured on top of a dispensed layer, there is difficulty in dispensing another layer without coming into contact with the calcium chloride solution, and immediately gelling. If the solution is sprayed on top of the dispensed layer, it is challenging to ensure the whole extruded layer will be gelled, without too much calcium chloride solution gathering at a specific location.

Even if the solution can be administered perfectly, the induced gelation is not very conducive to multi-layer part creation. Because calcium ions are freely available in the calcium chloride solution, the layer exposed to this solution will fully gel, leading to the next layer that is placed on top not adhering to the fully gelled layer below. The final part will separate into the layers in which it was constructed, known as delamination, and lose its integrity as a singular part. To properly build parts without delamination, the layer must be partially gelled to be solid enough to be built on top of, but still be able to adhere to the next layer.

As a result, for DBAM, there needs to be a way to introduce calcium ions to the sodium alginate ink after it has been extruded that is easy to administer, and leads to the part not being fully gelled. A method that accomplishes all these requirements will be investigated in the next part.

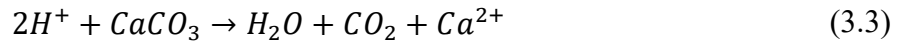
3.1.2 Crosslinking of Alginate with UV Light

Javvaji et al. [15] reported a possible solution that can accomplish the desired partial gelation, providing a framework for the ionic crosslinking of alginate using UV light, in a three-step process. The initial proposed ink has sodium alginate, mixed with a few additional components: calcium carbonate (CaCO_3), and a photoacid generator (PAG). The sodium alginate and photoacid generator dissolve into the ink to create a solution. However, at neutral pH, calcium carbonate is insoluble. As a result, the added calcium carbonate hangs in the ink as solid particles in a suspension. As the calcium carbonate remains solid, there are no calcium ions in solution available for the sodium alginate to react with.

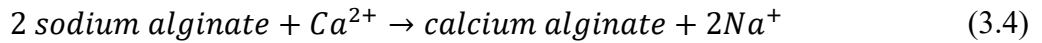
However, if this ink is exposed to UV light, the photoacid generator, as the name implies, reacts with the light to release hydrogen ions, causing the environment to become acidic, as summarized in Equation (3.2):



In more acidic environment, calcium carbonate becomes more soluble. The hydrogen ions released from the PAG will dissociate the calcium carbonate, releasing calcium ions, as seen in Equation (3.3):



The calcium ions released into the solution can react with the sodium alginate to cause crosslinking as seen in Equation (3.4), in the same reaction as Equation (3.1).



This new process can be easily implemented into DBAM. After the ink made of sodium alginate, calcium carbonate and photoacid generator has been extruded from a syringe, it can be exposed to UV light, to cause the reaction outlined above. The UV light is very easy to administer, with a UV lamp above the sample, requiring no contact. In addition, the original ink no longer is exposed to calcium ions readily available in solution. Instead, gelation requires three steps, and as a result is much slower and more controlled. It is much easier to achieve the desired partial gelation for between layers, by controlling the amount of UV light exposure. This UV light based technique has not been applied to DBAM yet, and so this project aims to develop this UV light-based gelation for DBAM.

3.1.3 Experimental Creation of Ink

Based on the UV-activated process outlined in the previous section, the ink will be a solution of sodium alginate, calcium carbonate and photoacid generator. Three materials, alongside calcium chloride, were used for the project. For the photoacid generator, Diphenyliodonium nitrate was selected. For the calcium carbonate, a nanopowder was chosen, as it would be more easily suspended in the liquid ink without affecting the ink's viscosity too much, or causing blockages in the needles when dispensed. Sodium Alginate (Product No: W201502), Calcium Chloride Dihydrate (Product No: 223506) and Diphenyliodonium Nitrate (Product No: 127396) were sourced from Sigma-Aldrich (Saint Louis, MO). Calcium Carbonate Nanoparticles (Product No: 1951RH) were sourced from Skyspring Nanomaterials (Houston, TX).

These inks were created by mixing the appropriate amount of each powder into distilled and deionized water. The specific concentrations chosen will be detailed in the following section. The solution was stirred for six hours using a magnetic stir bar, followed by ten minutes in an ultrasonic bath. These inks were stored in amber bottles to block out UV light during storage. Before expected use, the ink was placed for ten minutes in an ultrasonic bath once again, before being poured into amber syringes to be used with the machine.

3.1.4 Concentration Study

Having determined the composition of the ink to be used, the concentration of each elements must be determined. In their study of photo-activated ionic gelation of alginate, Higham et al. [16] uses concentrations of 4% w-v sodium alginate, 60mM PAG, and 30mM CaCO_3 . The ratios between the elements are selected for effective crosslinking. The 2:1 ratio of PAG to CaCO_3

corresponds to the stoichiometric ratio of 2 hydrogen ions to 1 calcium ion in the chemical equation, as seen in Equation (3.3). Similarly, they selected the ratio between CaCO_3 and sodium alginate based on estimates of how much of the sodium alginate will react with CaCO_3 .

However, while the chemical reaction determines the ratio between the elements, it does not determine the overall concentration level. A main property of interest for the ink is viscosity, which is strongly dependent on the concentration level of its components. If the viscosity is too low, the ink will flow after extrusion, causing distortion of recently extruded shapes. Conversely, at higher concentrations, there may be issues in the mixing process, and the final mixed ink may not be uniform. Different viscosities will also affect the width of a line extruded by the dispenser at a given pressure and needle diameter. As a result, it is necessary to determine the concentration level that would be best for the dispensing process.










To determine the ink that would result in the ideal viscosity, a study was set up to compare four different inks mixed with the same concentration ratios, but at different concentration levels. The concentrations used for the four inks can be seen in Table 3.1.

Observations were taken when the ink was mixed. Then, to see the effect on the width and integrity of the extruded shape, a circle of diameter 15mm was extruded from an air pressure controlled syringe through a needle of diameter 0.21mm, and photographed. These were extruded at 25, 50 and 75 psi to see how the different inks work at different pressure levels available from the dispenser. Pictures of these results can be seen in Table 3.2, including measurements of the average width of the line.

Table 3.1: Summary of concentrations of different inks used for concentration study.

Ink Number	Concentration of Sodium Alginate [% w-v]	Concentration of PAG [mM]	Concentration of CaCO₃ [mM]
1	4	60	30
2	6	90	45
3	8	120	60
4	10	150	75

Table 3.2: Pictures of 15mm circles extruded with the different inks at different pressure levels.

	Ink 1	Ink 2	Ink 3	Ink 4
25 psi	 Width: 3.06 mm	 Width: 1.05 mm	 Width: 0.61 mm	Extrusion is not constant
50 psi	 Width: 6.36 mm	 Width: 2.11 mm	 Width: 1.21 mm	Extrusion is not constant
75 psi	Too much ink to create shape	 Width: 4.17 mm	 Width: 1.72 mm	 Width: 0.54 mm

In order to allow for versatility with the dispenser later, the ideal ink should be able to work with a large range of pressures. From these pictures, Ink 4 in Table 3.2 is far too viscous, as it had trouble extruding at lower pressures. In addition, Ink 4 had some trouble with uniformity after the mixing process. By contrast, Ink 1 was not viscous enough, so that higher pressures dispense too much ink to be useful to make shapes with any decent resolution. In addition, the pictures of Ink 1 show quite a bit of distortion from the original circle, likely due to the lower viscosity ink flowing after it has been dispensed, which would result in error in the finally manufactured part. Ink 2 also exhibits some distortion from the original circle, especially at higher pressure levels. Ink 3 exhibits the least distortion of the original circle, while still being extrudable at multiple pressure levels.

Based on this study, the ideal concentrations are that of Ink 3: 8% w-v sodium alginate, 120 mM PAG and 60 mM CaCO_3 . The pressures to be applied will be investigated more closely in section 4.1. This is the ink composition that was used in the proposed work.

3.2 Modelling of Mid-layer Gelation

In the proposed method, the alginate ink is made solid via gelation. For the purposes of this project, partial gelation is necessary in between layers, to make the recently dispensed layer solid enough to support the next layer to be dispensed on top, but still liquid enough to be able to adhere to this next layer. If there is not enough gelation, the next dispensed layer will not sit on top of the previous layer, but instead mix with it. If there is too much gelation, the next layer will not adhere to the previous layer, leading to the layers in the final part separating through delamination. Because directly inducing gelation via calcium chloride solution leads to too much

gelation, it cannot be used for in between layers. As described in Chapter 3:, the proposed ink uses UV light to activate the gelation after it has been extruded. This gelation is a three-step process, and as a result is much slower, and the amount of UV exposure can be carefully controlled.

However, there is a need to determine the appropriate amount of UV exposure in between layers to achieve the correct amount of partial gelation. In addition to concerns with gelation, too much exposure to the heat from the UV lamp would result in water loss due to evaporation from the extruded ink. It is necessary to model the process to determine the ideal amount of UV exposure. Higham et al. [16] looked at the effect of intensity and exposure time on the gelation of alginate, but this was for much larger volumes of solution. Since in the context of DBAM, only a single thin layer is exposed to the UV light, their work cannot be applied. As such, there is a need for the effect of UV cure input parameters to be investigated in this context.

During the UV exposure process between layers, there are three main parameters that can be controlled: UV lamp intensity, exposure time, and thickness of the layer being gelled. In between layers, the partial gelation is necessary to support the next layer to be dispensed on top. To this end, an analysis of the mechanical properties of one layer after UV curing should reveal how much the layer strength has changed due to gelation. The proposed work in this section investigates the effect of UV curing intensity, exposure time and layer thickness on the mechanical properties of a layer after being exposed to UV light. Section 3.2.1 outlines the formation of the mechanical model that used. Section 3.2.2 outlines the design of the experiment to identify the model parameters. Section 3.2.3 gives details of the results of the experiments.

3.2.1 Formation of Mechanical Model

The rather viscous ink was modelled as a viscoelastic material – a material that has both elastic properties like a true solid, and viscous properties like a liquid. In modelling, elastic properties can be represented as a mechanical spring, while viscous properties can be represented as a mechanical damper. These two components can be combined to represent viscoelasticity in two different configurations. As seen in Figure 3.2, the Kelvin-Voigt model puts the components in parallel, while the Maxwell model puts in the elements in series [18].

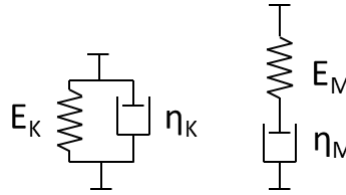


Figure 3.2: Representation of the Kelvin-Voigt (left) and Maxwell (right) models for viscoelasticity

Unfortunately, neither of these models can be used to capture the full mechanical response of the viscoelastic material to a stress. For a model that can better reflect the response of a viscoelastic material, the Kelvin-Voigt and Maxwell models can be put together in series to create the Burger model [19], seen in Figure 3.3.

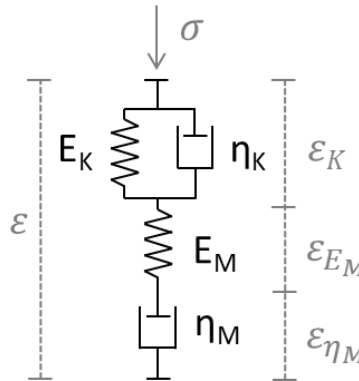


Figure 3.3: The Burger model for viscoelasticity, including applied stress σ and resulting strain response ε .

The individual parameters are labelled according the model they came from: E_M and η_M from the Maxwell model, and E_K and η_K from the Kelvin-Voigt model. To get a representation of the mechanical properties and response to stress of a viscoelastic material, the four Burger model parameters can be identified. Changes in the mechanical properties of the alginate ink after UV light exposure can be modelled by monitoring changes to the four Burger model parameters.

Looking at the Burger model representation in Figure 3.3, the response of the material to an applied stress σ can be derived. The theoretical expression over time can be derived by breaking down the total strain ε into component strains ε_{E_M} , ε_{η_M} , and ε_K : the strain in the Maxwell Elasticity, in the Maxwell Viscosity, and in the parallel Kelvin-Voigt model respectively.

$$\varepsilon = \varepsilon_{E_M} + \varepsilon_{\eta_M} + \varepsilon_K \quad (3.5)$$

The relation in the Laplace domain can be written between the applied stress ($\sigma(s)$) and response strain ($\varepsilon(s)$) using the different Maxwell Elasticity (E_M), Maxwell Viscosity (η_M), Kelvin-Voigt Elasticity (E_K), and Kelvin-Voigt Viscosity (η_K).

$$\varepsilon(s) = \frac{\sigma(s)}{E_M} + \frac{\sigma(s)}{s\eta_M} + \frac{\sigma(s)}{E_K + s\eta_K} \quad (3.6)$$

Creep is the expected change in strain with respect to time of a viscoelastic material under constant stress. Assuming constant applied stress σ_0 , an expression for $\sigma(s)$ can be written.

$$\sigma(s) = \frac{\sigma_0}{s} \quad (3.7)$$

Equation (3.7) can be substituted into Equation (3.6) to get an expression for the strain.

$$\varepsilon(s) = \frac{\sigma_0}{sE_M} + \frac{\sigma_0}{s^2\eta_M} + \frac{\sigma_0}{\eta_K s \left(s + \frac{E_K}{\eta_K}\right)} \quad (3.8)$$

Equation (3.8) can be converted to time domain via inverse Laplace Transform.

$$\varepsilon(t) = \left(\frac{\sigma_0}{E_M} + \frac{\sigma_0}{E_K}\right) + \frac{\sigma_0}{\eta_M}t - \frac{\sigma_0}{E_K}e^{-\frac{E_K}{\eta_K}t} \quad (3.9)$$

Equation (3.9) represents the expected strain response of the material under a constant stress based on the Burger model parameters.

3.2.2 Experimental Model Parameter Identification

To determine the Burger elasticities and viscosities for a given material, a simple experiment was designed to measure the strain response of a material under creep conditions. These measurements were then compared to the expected response in Equation (3.9) to fit for the different Burger parameters.

The set up for this experiment is seen in Figure 3.4. First, a single layer 25mm diameter solid circle of the ink was dispensed. Next the layer was exposed to UV at a given intensity for a given exposure time. These intensities and exposure times were varied to capture the properties under different UV exposure conditions. After exposure, a mass was placed on top of the exposed layer. A constraining frame ensured that the mass only moved in the vertical direction. The vertical position of the mass was measured by a laser displacement sensor, representing the thickness of the layer below as it changed due to creep. Figure 3.4b represents the position of the mass at the beginning of the experiment, when the measured thickness was equal to original

thickness T_0 . Figure 3.4c represents the position of the mass after measurement was completed, typically after 90 seconds.

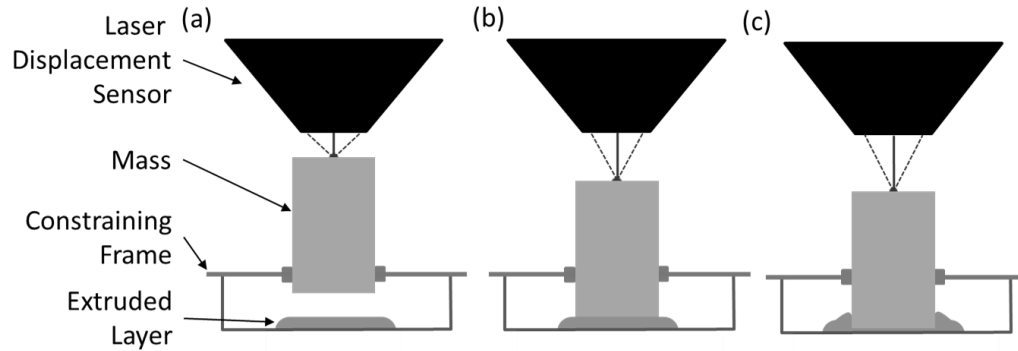


Figure 3.4: Experimental setup for Burger model parameter identification: (a) represents the general components; (b) represents the position at $t = 0$; (c) represents the position at the end of the experiment.

The Uvitron IntelliRay 600, a 600W UV flood lamp shown in Figure 3.5 is used to expose samples to UV light. The lamp has a cure area of 8 x 6 inches, corresponding to 200 x 150 mm. The lamp is placed 125mm above the bed where samples for curing are placed. An external electrical signal can be used to remotely open or close a shutter to regulate when the sample is exposed to UV light. The power intensity of the lamp can be manually adjusted between 35% to 100% of the full 600W lamp power.



Figure 3.5 Image of Uvitron IntelliRay 600 UV Flood Lamp [20]

To ease the identification of the model parameters from the experimental measurement, the creep strain time response was rewritten in terms of the experiment. The constant stress applied (σ_0) is a function of the mass (m) and cross-sectional area (A) of the object placed on the layer, as well as acceleration due to gravity (g).

$$\sigma_0 = \frac{mg}{A} \quad (3.10)$$

Similarly, the strain of the material as a function of time ($\varepsilon(t)$) can be written in terms of original thickness of the layer (T_0), and the measured thickness over time ($T(t)$).

$$\varepsilon(t) = \frac{T_0 - T(t)}{T_0} \quad (3.11)$$

The expressions for stress and strain can be substituted into the Equation (3.9).

$$\begin{aligned} \frac{T_0 - T(t)}{T_0} &= \frac{mg}{A} \left(\left(\frac{1}{E_M} + \frac{1}{E_K} \right) + \frac{1}{\eta_M} t - \frac{1}{E_K} e^{-\frac{E_K}{\eta_K} t} \right) \\ T(t) &= T_0 - \frac{mgT_0}{A} \left(\left(\frac{1}{E_M} + \frac{1}{E_K} \right) + \frac{1}{\eta_M} t - \frac{1}{E_K} e^{-\frac{E_K}{\eta_K} t} \right) \end{aligned} \quad (3.12)$$

The expression can be simplified using constant coefficients C_1 , C_2 , C_3 , and C_4 :

$$T(t) = C_1 - C_2 t + C_3 e^{C_4 t} \quad (3.13)$$

where:

$$\begin{aligned} C_1 &= T_0 - \frac{mgT_0}{AE_M} - \frac{mgT_0}{AE_K} \\ C_2 &= \frac{mgT_0}{A\eta_M} \\ C_3 &= \frac{mgT_0}{AE_K} \\ C_4 &= -\frac{E_K}{\eta_K} \end{aligned} \quad (3.14)$$

The expected thickness over time measurement based on Equation (3.13) is plotted in Figure 3.6. The response is an exponential that approaches a ramp asymptote. The effect of each of the constant coefficients can be noted: C_1 corresponds to the thickness of the exponential asymptote at time $t = 0$, C_2 corresponds to the slope of the ramp asymptote, C_3 corresponds to the amplitude of the exponential drop, and C_4 corresponds to the time constant of the exponential.

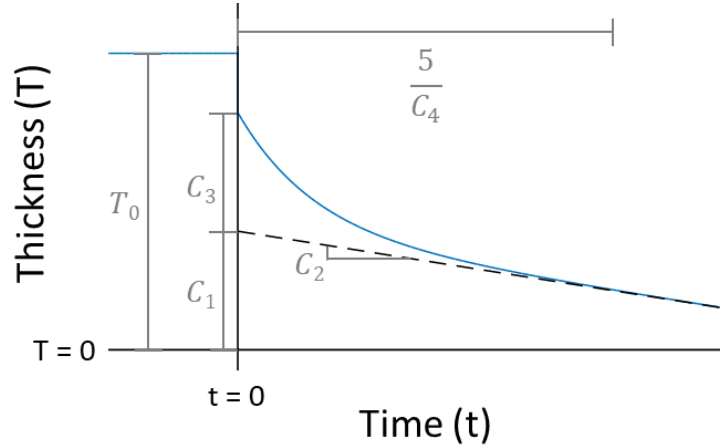


Figure 3.6: Expected response of a Burger model material to a constant applied stress.

Constants C_1 , C_2 , C_3 , and C_4 were determined by least squares fitting the experimentally collected thickness data to Equation (3.13). From these identified constants, and constant experimental parameters mass (m), cross-sectional area (A), acceleration due to gravity (g), and original thickness (T_0) the four Burger model parameters were calculated.

$$\begin{aligned}
 E_K &= \frac{mgT_0}{AC_3} \\
 \eta_M &= \frac{mgT_0}{AC_2} \\
 \eta_K &= -\frac{mgT_0}{AC_3C_4} \\
 E_M &= \frac{mgT_0}{A(T_0 - C_1 - C_3)}
 \end{aligned} \tag{3.15}$$

3.2.3 Experimental Results

The experiment outlined above was repeated for several samples, for a series of different input parameters.

- Layer Thickness: 0.55mm, 0.90mm
- UV Lamp Intensity: 35%, 50%, 75%
- Exposure Times: 0s, 45s, 60s, 90s, 120s

The Burger Model parameters E_K , E_M , η_K and η_M were calculated as outlined above. The test results are plotted in Figure 3.7 for the 0.55mm layer and Figure 3.8 for the 0.90mm layer.

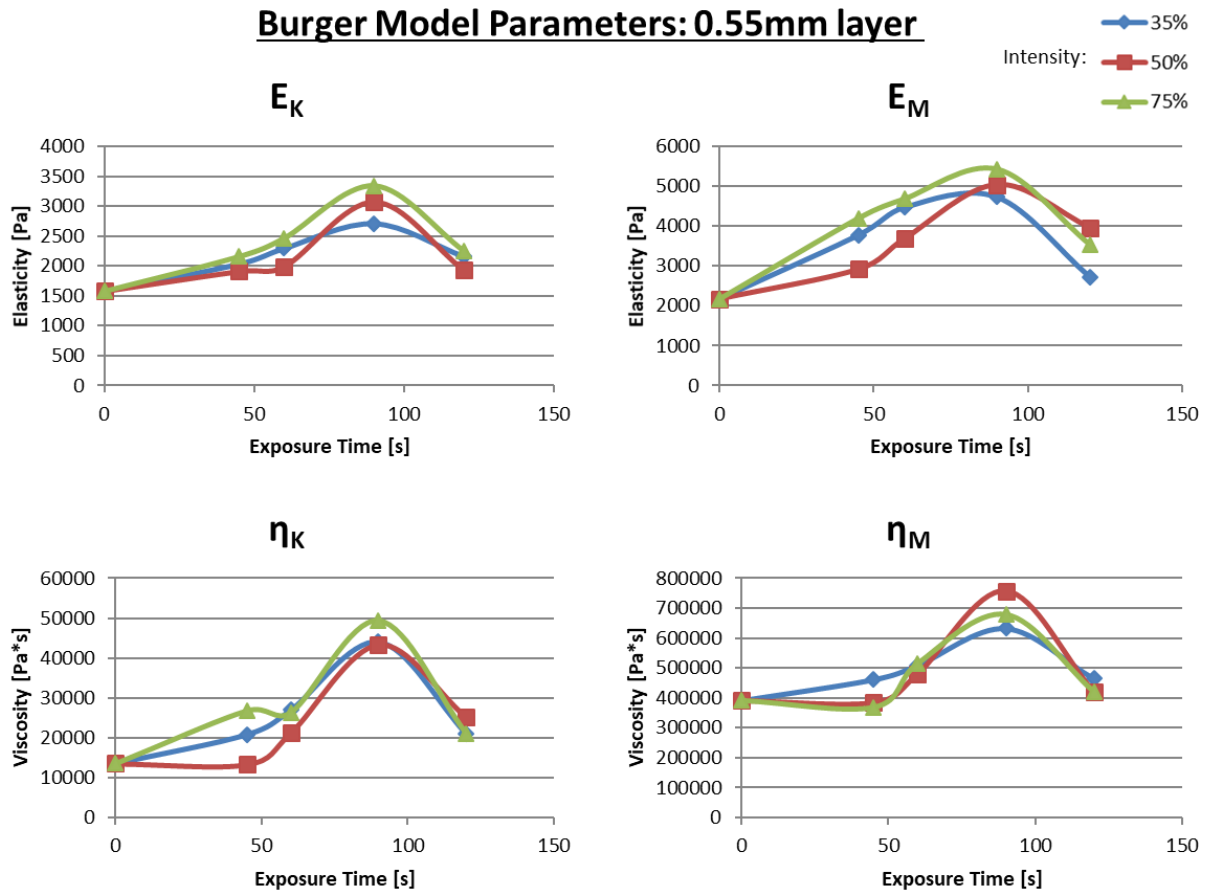


Figure 3.7: Identified Burger Model Parameters for single layer of thickness 0.55mm, where exposure time and lamp intensity are varied

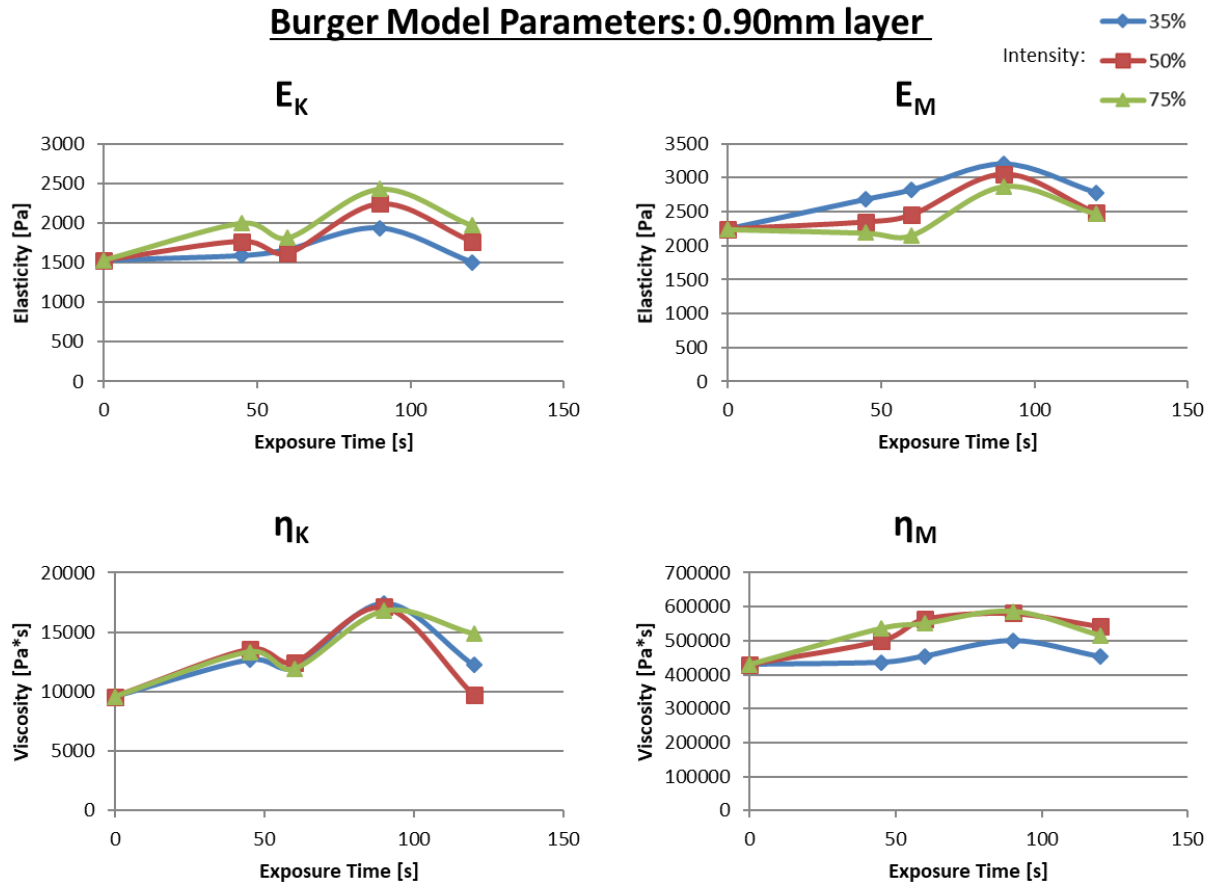


Figure 3.8: Identified Burger Model Parameters for single layer of thickness 0.90mm, where exposure time and lamp intensity are varied

In all cases, the four Burger Model parameters increase as exposure time increases, starting from 0 seconds up to about 90 seconds. This trend is expected, as more UV light exposure should lead to more crosslinking of the alginate, increasing the physical stiffness and the viscosity of the liquid. It seems in general that the intensity of the lamp does not have much of an effect on the mechanical properties. While the same trend is seen for both thicknesses, the larger thickness observes a smaller change in its parameters, likely because the UV hits mainly the surface of the

layer. For a thicker layer, the UV light would have a harder time penetrating through, resulting in parts of the bottom of the layer not crosslinking as much.

An initially unexpected result is the reversal of the trend at high exposure times above 90s. In all cases, all the Burger model parameters decrease as exposure time approaches the maximum value of 120s. This may be due to unwanted photodegradation of components of the ink. When first exposed to the UV light, the photoacid generator, Diphenyliodonium Nitrate, will break down into iodobenzene, phenol, nitrate and the hydrogen ion that is used for further reaction [17]. In literature, there are reports that iodobenzene and phenol both experience further photodegradation upon exposure to UV light [21], [22]. Both components are known to turn a yellow colour due to photodegradation. The case may be that initially, at low exposure times, the diphenyliodonium nitrate reacts with the UV light to activate the intended reaction. However, when much of the original PAG has reacted with the UV light, at higher exposure times, the byproducts start reacting with the UV light to result in unwanted photodegradation, which may interfere with the ionic bonding of the alginate and calcium ions, potentially inhibiting or breaking up crosslinks. Figure 3.9, shows pictures of the 0.55mm layer after exposure of different time lengths at 75%. The original ink is white, and at lower exposure times, such as at 45 seconds, this original uncured colour can be seen. However, at higher exposure times like 90s, a slightly darker yellow colour is seen, and a dark yellow is much more apparent in the final image for 120s curing. The yellowing of the ink points to the photodegradation of phenol and iodobenzene, which may be leading to the decrease of the Burger model parameters.

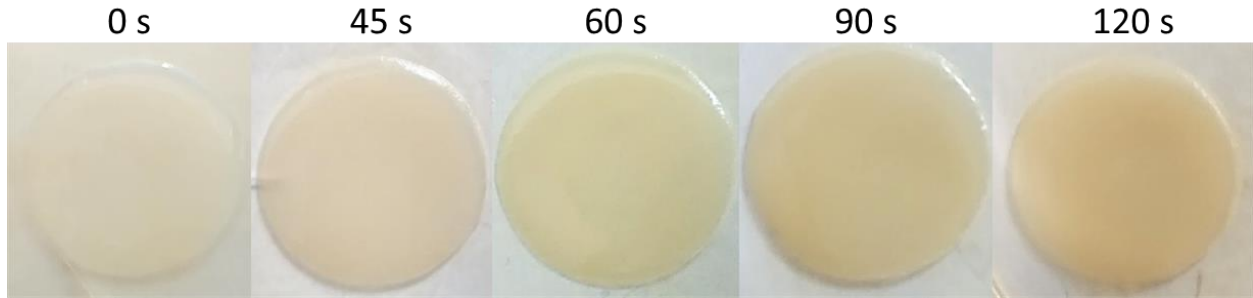


Figure 3.9: Pictures of 0.55mm layer after 75% intensity exposure of increasing times.

During the UV exposure, the lamp produced heat, which potentially causes unwanted evaporation of the water in the ink. To evaluate this possible water loss, the mass of the layer before and after exposure was measured for each of the samples. The average percentage mass loss was calculated for each input case, as summarized in Table 3.3. As expected, more mass loss is observed for higher exposure time, corresponding to longer time exposed to high temperature, and for higher intensity, corresponding to higher temperatures. Water loss is generally something to be avoided, as it can result in loss of total volume, changing the dimensions of the layer after exposure. Based on this, higher intensities and long exposure times are to be avoided.

Table 3.3: Measurement of mass loss for layer after UV exposure

Thickness [mm]	Intensity [%]	Exposure Time [s]			
		45	60	90	120
0.55	35	13.83%	15.11%	20.53%	21.41%
	50	15.57%	17.97%	22.31%	22.85%
	75	16.07%	18.09%	24.62%	29.63%
0.90	35	5.36%	6.83%	9.80%	10.89%
	50	7.66%	8.48%	10.65%	12.83%
	75	8.29%	9.90%	10.72%	13.08%

Based on these results, ideal parameters for the UV exposure can be determined. From the examination of the Burger model parameters, it seems that around 90 seconds of exposure, the maximum mechanical properties can be achieved, corresponding to the exposure time where the most UV activated crosslinking occurs, without too much disruption from photodegradation. Also, a thinner layer thickness would result in more effective crosslinking, based on the larger increase in mechanical properties for the 0.55mm layer. From the measurements of water loss, the lowest possible intensity of 35% should be used, especially since higher intensity does not cause much of difference in the mechanical properties. In summary, it seems that the most effective crosslinking is accomplished at a thickness of 0.55mm, intensity of 35%, and exposure time of 90s.

However, it is notable that while the mechanical properties achieved using these ideal parameters are suitable for the partial gelation between layers, they are not strong enough for a final solid part. In order to achieve full final gelation for a finally solid part, a post-processing step was added after the part has been fully built, where the part is immersed in a calcium chloride solution bath, leading to a desirable final full gelation for the manufactured part.

Chapter 4: Modelling and Control of Dispensing Step

As the ink has been finalized and gelation has been characterized, the dispensing step of DBAM can be investigated. In order to make a final part, the two-dimensional shape of each layer is dispensed, requiring a machine to move the syringe around, and the ink to be dispensed from the syringe. In this chapter, these two actions are investigated: Section 4.1 outlines the model used for the dispensing of the ink from the syringe, and Section 4.2 outlines techniques used to generate commanded machine movement.

4.1 Modelling of Dispensing Process

The ink is placed in the syringe, and the air pressure is applied to a stopper at the back of the syringe to push the ink out through a dispensing needle. The applied pressure, as well as the length and diameter of the needle can be controlled. In addition, the speed of the machine's movement of the syringe can be controlled.

As the syringe is moved and ink is extruded, a line of ink will be left behind. The width of this line is important to determine the resolution achievable under the given dispensing conditions, as well as to properly plan how the shape is filled out. The height of the fluid line is important to determine the height of a given layer. Both the height and width of the line is wholly dependent on the dispensing process. As a result, a model is necessary that would take the pressure, needle conditions and syringe speed as inputs and the predicted width and height as outputs. An overview of these inputs and outputs for the dispensing model can be seen in Figure 4.1. The model could also potentially be reversed, so that a desired output width or height can be used to calculate the necessary input parameters.

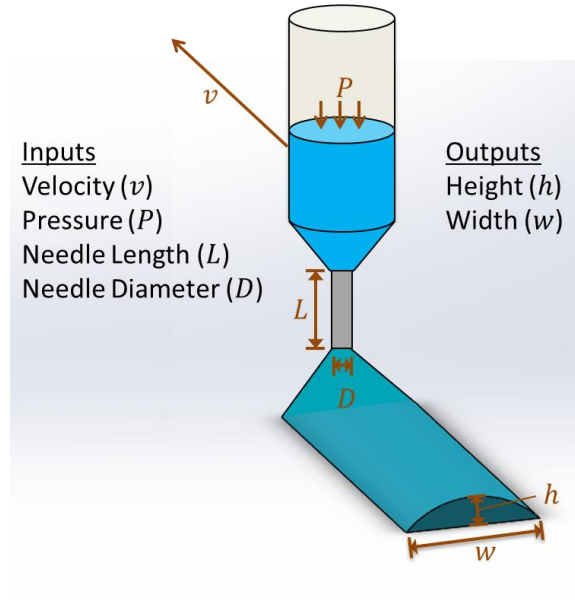


Figure 4.1: Illustration of inputs and outputs of the dispensing model.

This section follows the development of the model relating the input velocity, pressure, needle length and needle diameter to the output height and width. Section 4.1.1 adapts and rearranges a model presented by Khalil and Sun [10] for volume flow rate of a fluid through a needle. Section 4.1.2 outlines rheological measurements taken to identify important parameters of the model. Section 4.1.3 summarizes experiments made to validate the output flow rate mode. Section 4.1.4 shows modelling of the height and width of a deposited line based on the output flow rate.

4.1.1 Derivation of Flow Rate Model

An analytical expression was found in literature for the flow rate of a fluid through a thin passage like a needle. For a Newtonian fluid, Poiseuille's equation can be used to relate needle geometry, fluid viscosity and pressure gradient to the output flow. However, the ink that is being

used in this project is a shear-thinning non-Newtonian fluid, and so this expression cannot be used. Khalil and Sun [10] presents a modified form of the Poiseuille's equation for a non-Newtonian fluid. Here, volumetric flow rate output (Q) is modelled as a function of pressure (P), needle diameter (D), needle length (L), and fluid properties: power law index (n), and a specific viscosity (η_0) at low shear rate ($\dot{\gamma}_0$), as presented in Equation (4.1).

$$Q = \left(\frac{n}{3n+1}\right) \pi \dot{\gamma}_0^{\frac{n-1}{n}} \left(\frac{P}{L} \frac{1}{2\eta_0}\right)^{\frac{1}{n}} \left(\frac{D}{2}\right)^{\frac{3n+1}{n}} \quad (4.1)$$

Equation (4.1) can be rearranged to emphasize the effect of the input parameters. By taking the logarithm of both sides, and the expression can be rewritten as seen in Equation (4.2).

$$\log(Q) = \left(\log\left(\frac{n\pi\dot{\gamma}_0}{3n+1}\right) - \frac{1}{n}\log(2\eta_0\dot{\gamma}_0)\right) + \frac{1}{n}\log\left(\frac{PD}{2L}\right) + 3\log\left(\frac{D}{2}\right) \quad (4.2)$$

The constant terms, can be grouped together in order to simplify the expression. As the same ink is always used, the fluid properties can be treated as constant terms as well. Some grouping and rearranging leaves an expression in terms of the relevant input parameters of pressure, needle diameter and needle length, and two constant model parameters a and b , seen in Equation (4.3):

$$\log Q = a + b \log\left(\frac{PD}{2L}\right) + 3\log\left(\frac{D}{2}\right) \quad (4.3)$$

Where:

$$a = \left(\log\left(\frac{n\pi\dot{\gamma}_0}{3n+1}\right) - \frac{1}{n}\log(2\eta_0\dot{\gamma}_0)\right) \quad (4.4)$$

$$b = \frac{1}{n}$$

4.1.2 Calculating Model Parameters via Rheological Measurement

In order to continue with this model, the parameters a and b must be identified. Since they are functions of constants and material properties, they can be calculated if the material properties are measured. The necessary material properties are power law index (n), a specific viscosity (η_0) at a specific shear rate ($\dot{\gamma}_0$), based on the power-law model for fluid, which gives viscosity (η) as a function of shear rate ($\dot{\gamma}$), consistency coefficient (K) and power law index (n_p):

$$\eta = K\dot{\gamma}^{n_p-1} \quad (4.5)$$

The power law index n from Khalil and Sun's model is equal to n_p from power-law model here. The specific viscosity η_0 and specific shear rate $\dot{\gamma}_0$ are defined as a viscosity and shear rate pair that satisfies this relationship. Using the power law model, the relationship between shear rate and viscosity is expected to be a straight line on a logarithmic plot.

Using the TA Instrument AR 2000 Rheometer, the viscosity of the ink was measured over a wide range of shear rates in order to determine these non-Newtonian rheological properties. The results of the sweep can be seen in the logarithmic plot in Figure 4.2. The ink is clearly non-Newtonian, as the viscosity changes significantly as the shear rate changes. Specifically, the ink was identified as shear-thinning, as viscosity drops with an increase in shear rate. However, the expected straight line relationship is not seen here, indicating that the power-law fluid model is not sufficient to describe the shear behavior of the ink. Looking closer, the data seems to converge to a straight line at higher shear rates, but converges to a specific viscosity value at lower shear rates.

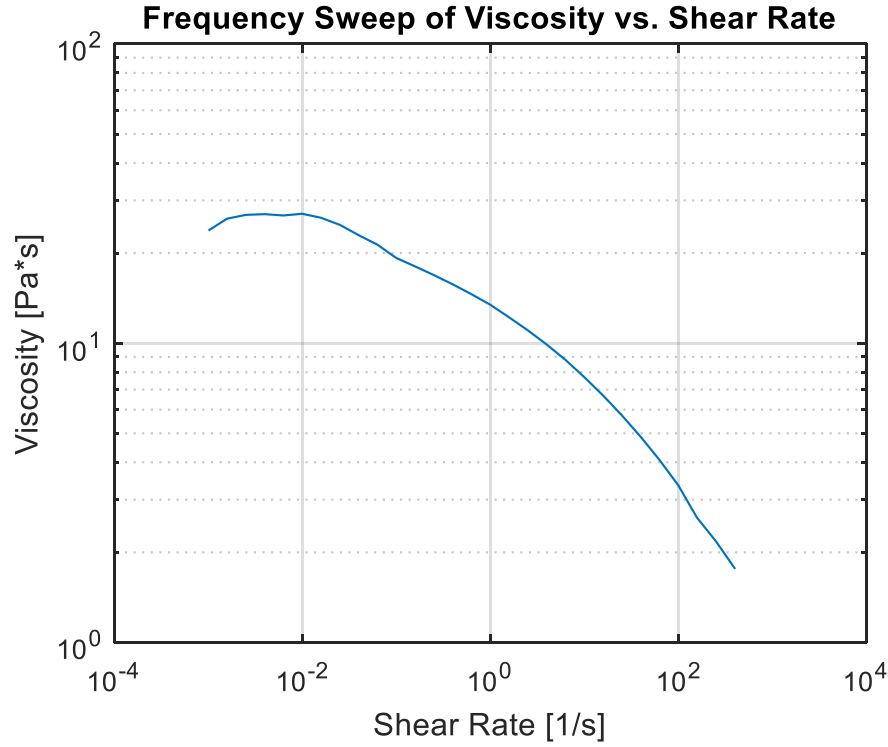


Figure 4.2: Measurement of viscosity of ink at different shear rates at different frequencies

To more accurately fit the measured data, the more complex cross fluid viscosity model was used. The cross fluid model shows a different relationship between viscosity (η) and the shear rate ($\dot{\gamma}$) with addition parameters: zero shear viscosity (η_0), infinite shear viscosity (η_∞), cross rate constant (m_c) and cross time constant (C):

$$\eta = \eta_\infty + \frac{\eta_0 - \eta_\infty}{1 + (C\dot{\gamma})^{m_c}} \quad (4.6)$$

In order to differentiate the cross model zero shear viscosity from the flow rate model specific viscosity, zero shear viscosity will be labelled η_{0C} .

If the cross model were to be plotted on a logarithmic plot, the viscosity converges to the zero shear viscosity η_{0C} at low shear rates, and to the infinite shear viscosity η_∞ at high shear rates. In

between, the relationship resembles a straight-line like the power-law model. In the data from the experimental measurement, convergence to a value was observed for low shear rates, but not for high shear rates. As such the high shear rate convergence can be set to be infinitely far by setting $\eta_{\infty} = 0$, allowing the cross model to be simplified.

$$\eta = \frac{\eta_{0C}}{1 + (C\dot{\gamma})^{m_c}} \quad (4.7)$$

This is the form of the cross model that will be used going forward.

In the case that $(C\dot{\gamma})^m \gg 1$, as would occur at high shear rates, the expression can be simplified:

$$\begin{aligned} \eta &= \frac{\eta_{0C}}{(C\dot{\gamma})^{m_c}} \\ \eta &= \frac{\eta_{0C}}{C^{m_c}} \dot{\gamma}^{-m_c} \end{aligned} \quad (4.8)$$

This form is clearly a rearrangement of the power law model, where:

$$\begin{aligned} K &= \frac{\eta_{0C}}{C^{m_c}} \\ n_p &= 1 - m_c \end{aligned} \quad (4.9)$$

The relationships in Equation (4.9) confirm that this version of the cross model simplifies to the power-law model at high shear rates, allowing for connection to be made between the parameters of the cross model to the those of the power-law model where the two models converge.

The simplified cross model can be fitted to the measured data from the rheometer, as seen in Figure 4.3. This fit gives the cross model parameters: $C = 0.8141$, $\eta_{0C} = 27$ and $m_c = 0.4585$.

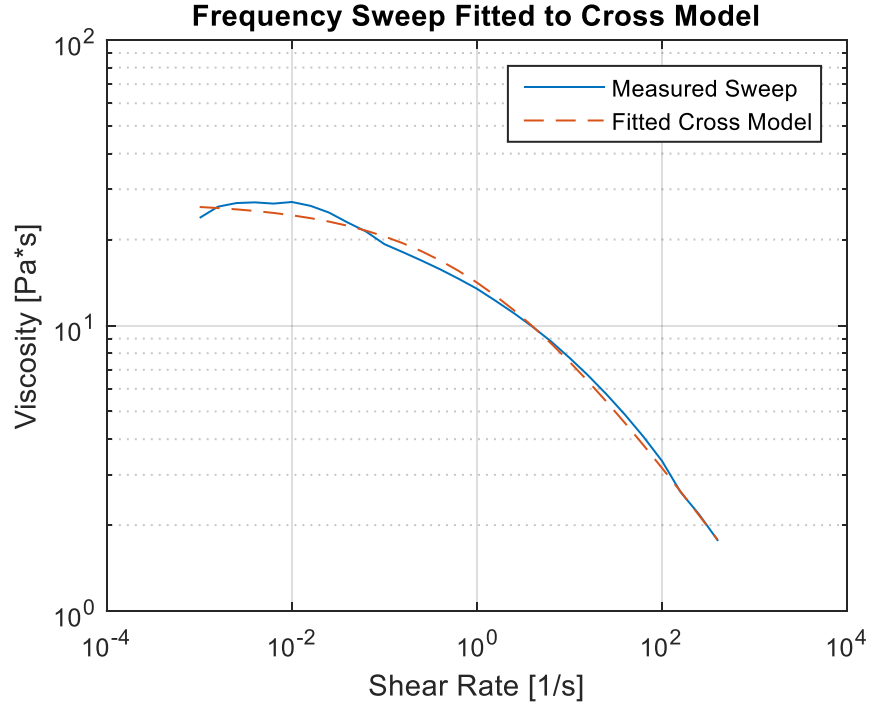


Figure 4.3: Fit of the cross model to the measurement data.

The value for the important rheological parameters can be derived from the fit cross model. Power law index n can be derived from cross model parameter m . The specific viscosity η_0 and specific shear rate $\dot{\gamma}_0$ can be taken from the highest shear rate point, where the data most closely follows the power-law model. This gives us the following important material parameters:

$$n = 0.5415; \eta_0 = 1.7804; \dot{\gamma}_0 = 398.1 \quad (4.10)$$

From these values, the constant parameters a and b can be calculated:

$$a = -7.8488; b = 1.8468 \quad (4.11)$$

4.1.3 Experimental Validation of Flow Rate Model

An experiment was set up to validate this flow rate model, including the parameter values derived from the rheometer measurements. Under different pressure and needle conditions, the flow rate from the extruder was measured, and compared to the predicted value from the model.

The Techcon TS350 Digital Fluid Dispenser is used to dispense the ink. A summary of this system is shown in Figure 4.4. It operates by applying air pressure, controlled by a base unit, to a stopper inside a syringe to push the ink inside through a needle. The pressure of the air applied can be manually adjusted to any value between 0 to 80 psi, corresponding to 0 to 550kPa. When using the dispenser, the application of the pressure is turned on or off via an external electrical signal in.

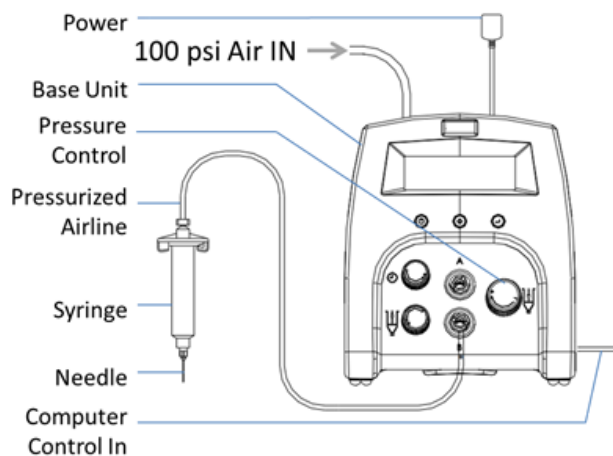


Figure 4.4 Summary of Techcon TS350 Digital Fluid Dispenser [23]

The syringes used are amber coloured to block out UV light, so the ink inside will not be exposed. A stainless steel Luer-Lok needle is attached to the end of the syringe. Needles of different diameters and lengths are available depending on the application.

To measure the flow rate under different conditions, the ink is placed into a syringe, and a needle with a given diameter (D) and length (L) was installed. A given pressure (P) was applied for a dispense time (t_d) of five seconds, and the mass dispensed (m_d) is measured. The mass was converted to volumetric flow rate (Q) based on the dispense time and the density of the ink (ρ):

$$Q = \frac{m_d}{t_d \rho} \quad (4.12)$$

The data was used to experimentally identify parameters a and b via least squares fitting. In this way these parameters were identified as $a = -7.096$ and $b = 1.8274$, which is very close to the previous calculated values based on the rheometer measurements.

In Figure 4.5, a comparison was made between the flow rate predicted using the calculated values for a and b , flow rate predicted using the experimentally fit values for a and b , and the experimentally measured flow rate. All three sets of data are very close, validating both the model used, and the calculated parameters a and b .

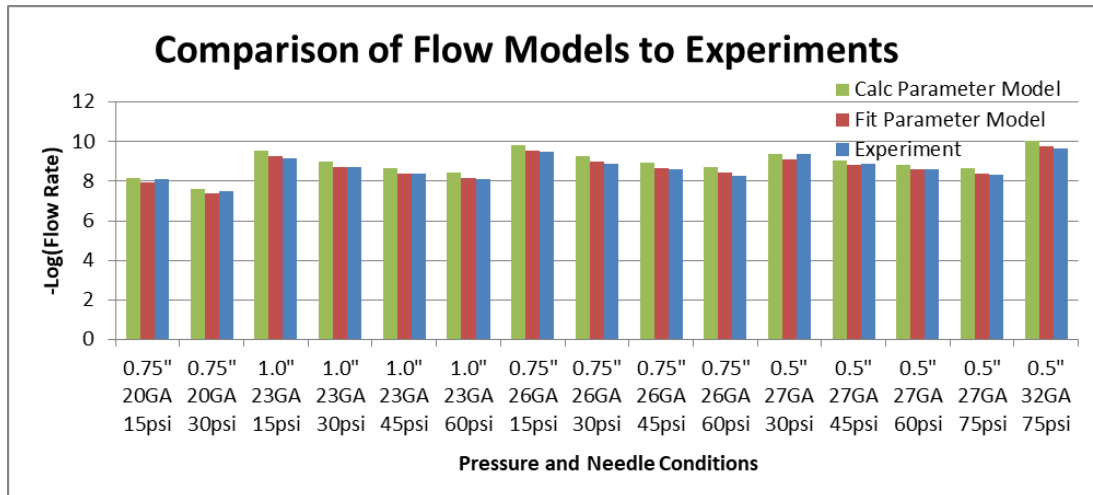


Figure 4.5: Comparison of predicted flow rate using the calculated parameters, predicted flow rate using experimentally fit parameters, and the experimentally measured flow rates.

4.1.4 Modelling of Deposited Height and Width

The flow rate model needs to be further extended to determine the height and width of a line that would be dispensed from the syringe. Firstly, the cross section area for a dispensed line (A_d) can be calculated from the volumetric flow rate (Q) and the movement speed of the syringe (v):

$$A_d = \frac{Q}{v} \quad (4.13)$$

The liquid ink deposited in a line, and the cross sectional area can be modelled as a circle section, as seen in Figure 4.6. There are three important parameters to the circle section: height (h), width (w) and contact angle (θ). The contact angle is based on the properties of the solution, and of the surface it is sitting on. By geometry, the height and width can be calculated from the cross sectional area and contact angle.

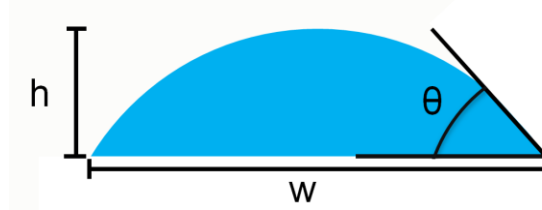


Figure 4.6: Representation of the circle section cross sectional area.

An intermediate term R can be defined as the radius of the circle from which the section is taken.

The dispensed cross sectional area A_d can be defined as a function of R and contact angle θ :

$$A_d = \frac{1}{2} R^2 (2\theta - \sin 2\theta) \quad (4.14)$$

The width and height can be written as function of the θ and R :

$$\begin{aligned} w &= 2R \sin \theta \\ h &= R(1 - \cos \theta) \end{aligned} \quad (4.15)$$

By substituting an expression for R derived from Equation (4.14) into Equation (4.15), an expression for width and height can be written in terms of cross sectional area and contact angle:

$$w = 2 \sin \theta \sqrt{\frac{A_d}{\theta - \sin \theta \cos \theta}}$$

$$h = (1 - \cos \theta) \sqrt{\frac{A_d}{\theta - \sin \theta \cos \theta}}$$
(4.16)

As both height and width are functions of the contact angle and cross sectional area, an expression can be made directly relating the height to the width:

$$h = \frac{1}{2} w (\csc \theta - \cot \theta)$$
(4.17)

From observation of experimental results, the contact angle was approximated to 45° for the ink and plastic petri dishes used, allowing the value for contact angle to be substituted into the expressions above. Most notably, substituting $\theta = 45^\circ$ into Equation (4.17), gives a constant relationship between the dispensed height and the dispensed width:

$$h \cong 0.207w$$
(4.18)

Thus, the width is expected to be approximately five times the height for a dispensed line.

By stringing the flow rate model presented in Equation (4.3) with the expression for width and height in Equation (4.16), a full expression can be written for height (h) or width (w) in terms of identified constants of contact angle θ , a , b , and user input parameters movement speed (v), pressure (P), needle diameter (D), and needle length (L).

$$\begin{aligned}
w &= \sin \theta \sqrt{\left(\frac{e^a D^3}{2v(\theta - \sin \theta \cos \theta)}\right) \left(\frac{PD}{2L}\right)^b} \\
h &= (1 - \cos \theta) \sqrt{\left(\frac{e^a D^3}{8v(\theta - \sin \theta \cos \theta)}\right) \left(\frac{PD}{2L}\right)^b}
\end{aligned} \tag{4.19}$$

Of the highlighted input parameters, the pressure is easiest to tune on the digital dispensing system. As a result, Equation (4.19) can be rearranged to calculate the required pressure to achieve a desired layer height based on the needle properties and other identified parameters:

$$P = \frac{2L}{D} \left(v e^{-a} \left(\frac{h}{2(1 - \cos \theta)} \right)^2 \left(\frac{D}{2} \right)^{-3} (\theta - \sin \theta \cos \theta) \right)^{\frac{1}{b}} \tag{4.20}$$

4.2 Trajectory Generation

After the process has been modelled, algorithms are necessary to determine how the machine should be commanded to move to create a manufactured part. Ultimately, the goal is to have a desired part defined in three-dimensional Computer Aided Design (CAD), and for a set of algorithms to generate the necessary trajectory. The method that is outlined in this chapter is an adaptation of work by Sencer et al. [24], expanded by Yuen et al. [25]. The general overview of the trajectory generation method can be seen in Figure 4.7. Section 4.2.1 details the steps taken to convert the 3D models into 2D by use of the commercial software Slic3r [26], generating a set of points that the machine must traverse. Section 4.2.2 details the steps taken to convert the set of 2D layer of points into a 2D spline, giving a continuous toolpath that for the machine to follow. Section 4.2.3 details the conversion of the 2D spline toolpath into a time-based trajectory, including optimization of tangential feed rate to minimize traversal time while limiting velocity,

acceleration and jerk, giving a trajectory of positions with respect to time. Section 4.2.4 details the synchronization of the extrusion from the dispensing system with the trajectory velocity to ensure that the layer lines are of even width. Lastly, section 4.2.5 details some experimental results validating the effectiveness of these trajectory generation techniques.

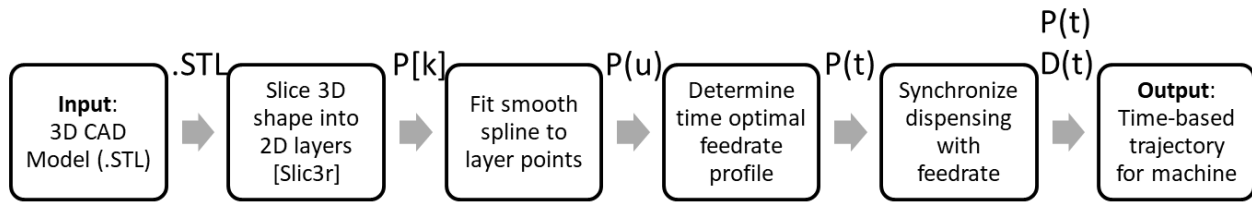


Figure 4.7 Overview of trajectory generation method in this chapter.

4.2.1 Slicing of 3D Models

The first step is to convert the input 3D model into multiple 2D slices so that the 3D shape can be built additively, layer by layer. There exist many tools already developed for the purpose, mainly for the much more popular Fused Deposition Modelling (FDM) style of Additive Manufacturing. One such tool is used in this work: Slic3r [26].

Slic3r takes a 3D CAD model in .STL format, and slices it into discrete two dimensional layers it according to a few important parameters. The input of a simple cube shape into the software can be seen in Figure 4.8. The most important parameter affecting the slicing is the desired layer height, which ultimately determines the number of slices to be taken, and the resulting resolution. Once the layer height is established, Slic3r will slice the 3D object into the necessary number of slices.

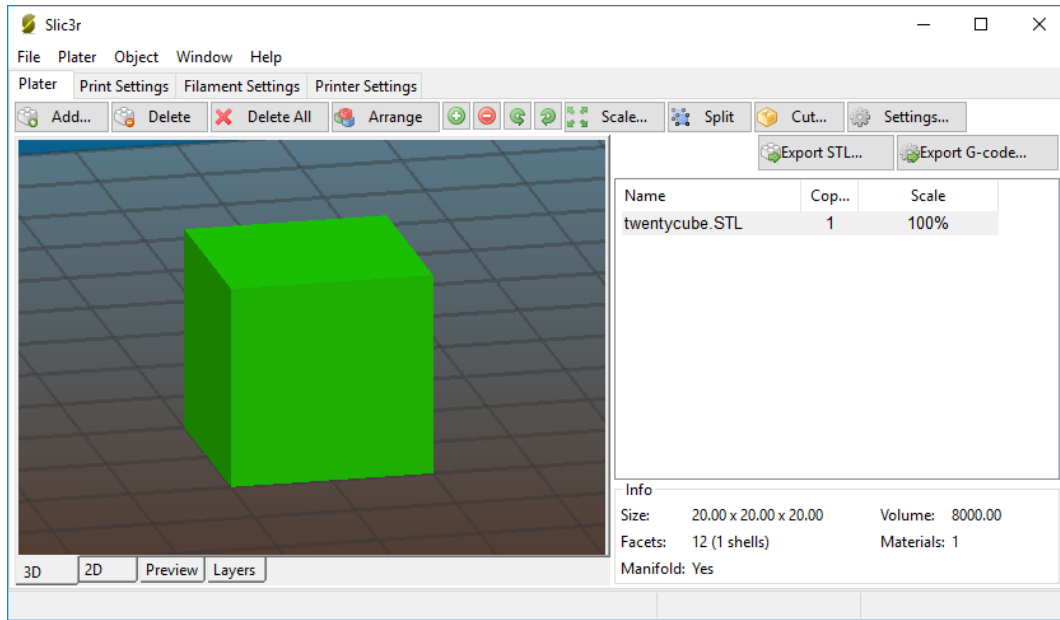


Figure 4.8 Input of a cube with side length 20mm into Slic3r.

Once the slicing has been accomplished, Slic3r outlines the perimeter of the shape. The next critical task for Slic3r is to generate infill, which are paths through the inner area of the 2D layer to fill out volume that is meant to be solid. To create this infill, Slic3r uses two important parameters: fill pattern, and fill density. The fill pattern used for this project is rectilinear, filling the inner area with a set of parallel lines through the centre of the shape, connected at the ends. A given layer's infill lines are arranged perpendicular to the infill lines of the layer beneath it, creating a final part with a square hatch pattern for the solid volume, which is useful for generating predictable porosity and strength properties.

The fill density is inputted as a percentage and must be carefully tuned for the purposes of the alginate bone scaffolds. Since Slic3r was designed for FDM, it assumes the cross-section shape of an extruded line to be circular or elliptical. However, based on the dispensing model from

Section 4.1, DBAM produces a circle segment cross-section, resulting in a line that is much wider than Slic3r would predict for a given height. To offset this increased width, the inputted fill density into Slic3r must be compensated lower than the desired final part porosity.

A sample layer including the generated infill for the cube shape can be seen in Figure 4.9. The Slic3r takes all the layers it generates to create a G-code file for an FDM machine to use. The G-code features a set of points that must be traversed, and commands straight line movements between these points.

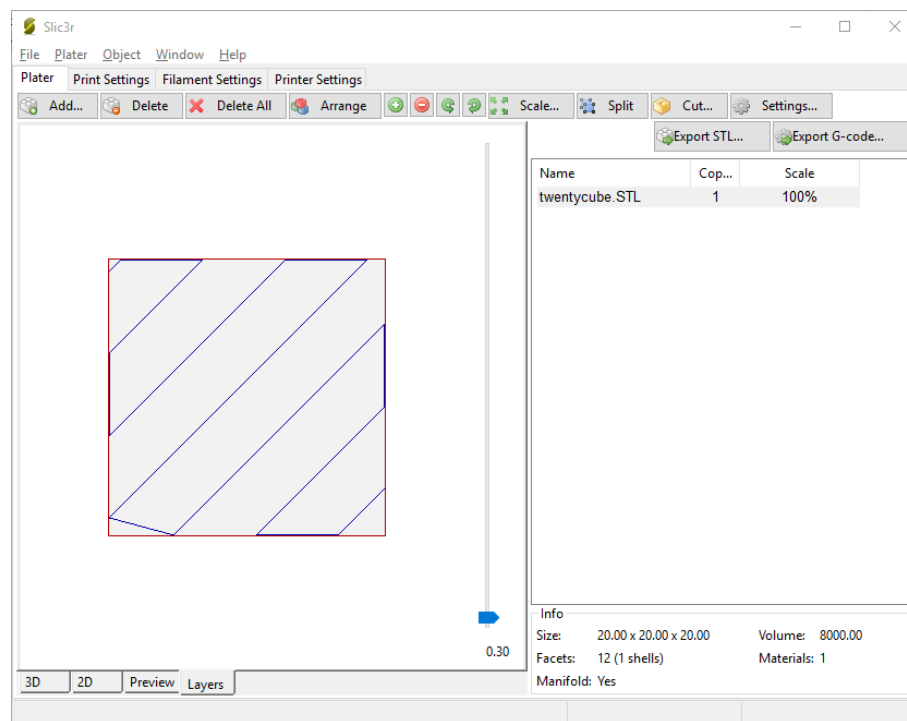


Figure 4.9: Layer with infill created by Slic3r for the simple cube shape.

4.2.2 Creation of 2D Toolpath

The G-code provided by Slic3r commands a straight-line path at a set speed between the points of interest in a layer. A straight-line path in two dimensions results in non-continuous speed,

requiring infinite acceleration to start and stop moving, and to change directions. Since no machine is capable of infinite acceleration and deceleration, errors occur at the start and stop of paths, and corners. In addition, discontinuous accelerations sent to the motor can lead to unwanted vibrations.

To reduce these sources of error, trajectory generation techniques from Yuen et al. [25] were applied. The first step is to create a quintic B-spline that goes through the points from the G-code. Compared to the straight-line path given by the G-code, this smooth splined path has continuous velocity, acceleration and jerk, eliminating previously identified sources of error.

Yuen et al. derived a method to find a spline that would pass through a set of given points. However, since the path suggested by the G-code feature a lot of long straight lines, the identified points are far apart. Trying to fit a spline to these points results in a spline whose curves significantly deviate from the intended straight-line path. To generate a spline closer to the intended path, the points from the G-code were interpolated in between so that there is no more than 1mm distance between successive points along the path. Seen in Figure 4.10 is an example of interpolation for the infill of one layer of the cube. These new set of points can then be used to fit a quintic B-spline that closely follows the intended path.

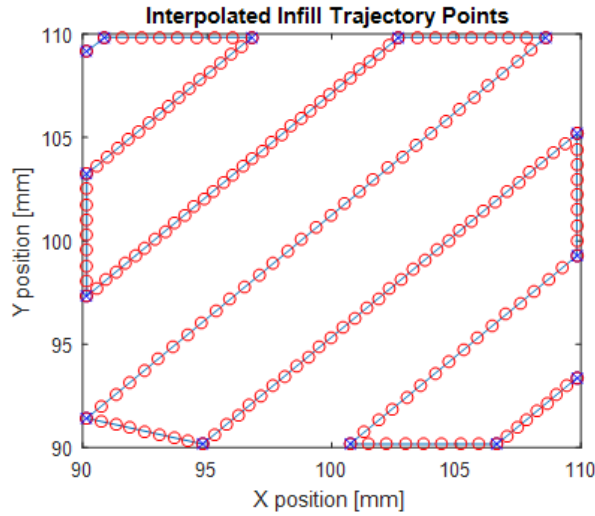


Figure 4.10: Interpolation of pass-through points to create spline. Blue x's represent the original points from G-code, and red circles represent the new interpolated points.

The spline fitted to the points from Figure 4.10 can be seen in Figure 4.11. The fitted spline follows the original path quite closely. However, it can be seen at sharp changes in directions, the spline will create a curve that allows for continuous change in velocity, acceleration and jerk that the machine would be able to handle. A spline parameter u is used to define the generated two-axis spline $P(u)$, where $u = 0$ at the start of the path, and $u = 1$ at the end of the path.

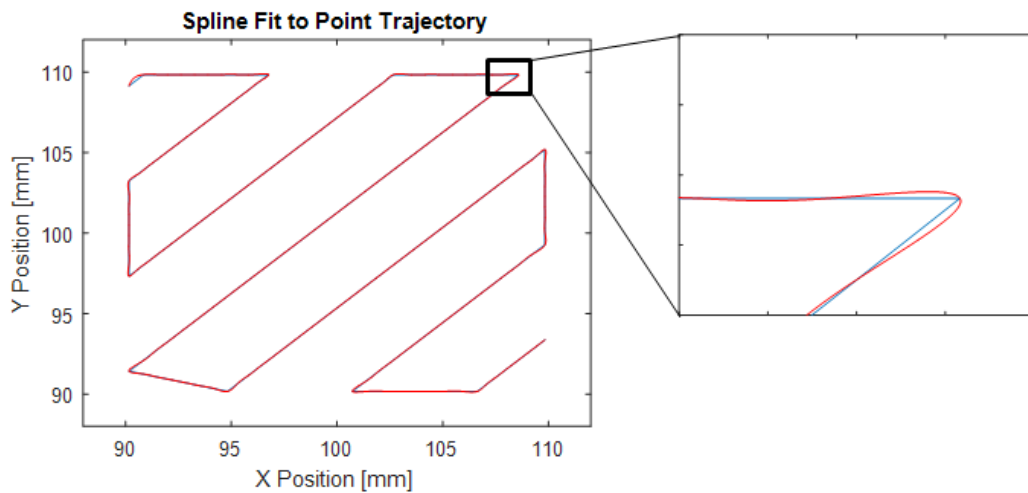


Figure 4.11: Spline fitting: original path from the G-code is seen in blue, and the new fitted spline is in red.

4.2.3 Feedrate Optimization

While the spline represents the desired toolpath to follow, this toolpath must be written as a function of time to be fed into the controller. First, the spline, initially written in terms of spline parameter u , must be written in terms of path displacement s . The relationship between u and s is not necessarily linear, according to Yuen et al [25]. Therefore, a spline polynomial, known as a feed correction spline, is calculated to determine $u(s)$, allowing the toolpath to be written as function of the displacement along its path: $P(u(s))$.

To convert from position with respect to the path to position with respect to time, it is necessary to determine the tangential speed as the machine travels the toolpath, known as feedrate. Sencer et al. [24] suggested using a non-uniform spline for the feedrate, using an optimizer to strategically modify the feedrate at different points along the path in order to minimize the time taken to traverse the toolpath, while respecting applied limits for velocity, acceleration and jerk for each axis. The optimization is accomplished by using the `fmincon` function in MATLAB, where the objective function to minimize is an expression for total trajectory time, and the constraint function are the desired maximum movement speed as a velocity, and axis specific limits for the acceleration and jerk. In Figure 4.12, the optimized feedrate spline for the infill toolpath can be seen. The velocity limit was set as 10 mm/s, and so the feedrate tries to drive at 10mm/s as much as possible to minimize the traversal time. The noted dips in the feedrate correspond to tight acute angled corners in the toolpath. Sharp corners are where high acceleration and jerk are expected, and so the speed is dropped to stay within the applied limits.

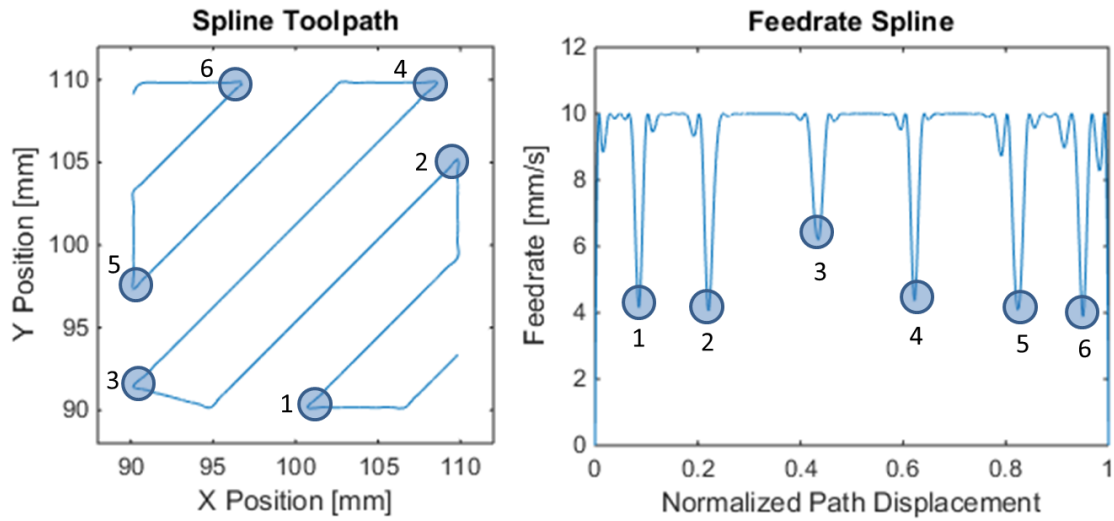


Figure 4.12: For spline toolpath on the left, the calculated feedrate spline on the right. Dips in the feedrate spline correspond to sharp turns in toolpath.

Using the generated feedrate profile, position for each time sample can be generated by moving down the toolpath spline a specific distance based on the feedrate at that point. By continuing through the layer's full toolpath, the commanded X, Y and Z positions are now available with respect to time.

4.2.4 Synchronized Dispensing

With a non-uniform optimized feedrate profile, the speed at which the syringe is moved is no longer constant. However, as seen before in the dispensing model from Section 4.1, the speed of the syringe movement is an important parameter that affects the width of the line being extruded. It is important that the deposited width be held uniform, so that no part is thicker than originally intended. More importantly, the width is very closely related to the height, and inconsistencies in the height will propagate and accumulate as the part is built up layer by layer. As a result, the dispensing width and height must be kept constant despite changes in velocity.

While the pressure is the easiest parameter to change in the dispensing process, the dispensing system being used does not allow for the pressure to be changed during operation. The only input to the dispensing system that can be dynamically controlled by the dSPACE control board to adapt for the changes in the velocity would be the signal to turn the dispensing on or off. The amount of fluid dispensed can be controlled by affecting this signal using Pulse Width Modulation (PWM). When PWM is applied, the effective fluid volumetric flowrate from the dispenser (Q_{eff}) is directly proportional to PWM duty cycle d . An expression for the effective volumetric flow rate with respect to the duty cycle can be written.

$$Q_{eff} = d \cdot Q_{theoretical} \quad (4.21)$$

The model for width from Section 4.1, Equation (4.19) can be expanded to include duty cycle d .

$$w = \sin \theta \sqrt{d \left(\frac{e^a D^3}{2v(\theta - \sin \theta \cos \theta)} \right) \left(\frac{PD}{2L} \right)^b} \quad (4.22)$$

In Equation (4.22), it can be seen that varying the duty cycle to stay directly proportional to changing movement velocity would result in the width staying uniform, as all of the other parameters stay constant. The maximum velocity that is used to generate the time trajectory can be mapped to 100% duty cycle, and then the duty cycle can then be reduced proportionally to any reduction in from maximum velocity, resulting in the duty cycle profile for a trajectory becoming a normalized version of the velocity profile. The duty cycle value for each sampling point in the trajectory is fed into the dSPACE alongside the commanded position.

4.2.5 Experimental Validation of Trajectory Generation Techniques

These trajectory generation techniques were tested on a 3-axis CNC machine in the Manufacturing Automation Laboratory that was adapted for DBAM, pictured in Figure 4.13.

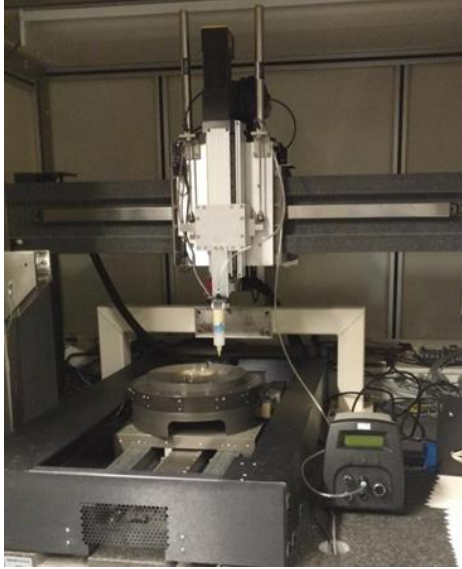


Figure 4.13 Image of 3-axis CNC machine

Motion in horizontal directions are handled by the X and Y axes. X and Y movement is actuated using linear motors, and supported by air bearings driving over granite rails, resulting in very low friction to achieve high precision. The X-axis, is implemented as a gantry axis, seen in Figure 4.13 and has 800mm of available stroke length. The Y-axis, is seen driving on the granite base of the machine, and has a stroke of approximately 450mm.

Vertical motion is handled by the Z-axis drive. The Z-axis is mounted on the X-axis and moves along the gantry. In contrast to the X and Y axes, the motion in the Z direction is actuated by a rotary DC motor, driving a lead screw actuator. The lead screw ensures that the drive is not back-drivable, and so external forces acting on the stage, like gravity, cannot cause motion in Z. An air

cylinder is added to offset gravity, so that the same amount of force is required from the drive for similar movements upward or downward. The syringe from the digital dispenser is mounted to the Z-axis, while a plastic petri dish is placed as a built base on the Y-axis allowing the syringe to move in three axes with respect to the base and extrude the ink onto the petri dish to build.

The control and synchronization of the machine is handled by a dSPACE 1103 controller board. A custom designed control structure is uploaded to the controller, which can operate at 10kHz to execute commands from a PC. The uploaded control structure includes a closed-loop motion control system that sends commands to the motors via the machine's power amplifiers. Each axis has a PI controller with a lead filter, designed such that all three axes would have matched dynamics, as seen in Figure 4.14, exhibiting a 25Hz bandwidth, and a 60 degree phase margin to allow for robust control. In addition, the dSPACE is responsible for sending the previously described on and off signals to the dispenser and the UV lamp, appropriately coordinated with the other commanded movements.

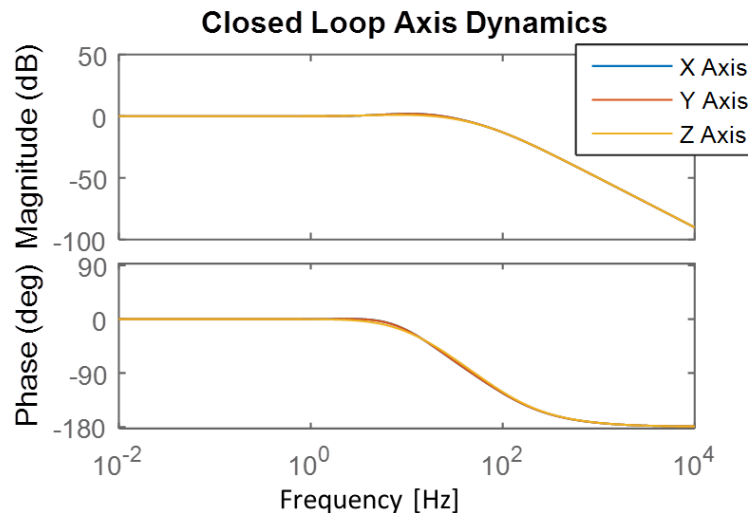


Figure 4.14 Bode Plot showing Matched Motion Axis Dynamics of the three axes

Finally the PC interaction with the dSPACE is set up such that the machine can be fed a user defined trajectory that include commanded X, Y and Z positions as well as dispenser on/off status and dispenser duty cycle for all time points at a 10kHz sampling time for the length of the trajectory.

To validate the trajectory generation techniques outlined in this chapter, the path seen in Figure 4.12 was sent to the machine. First a constant speed trajectory along the straight-line path commanded by the G-code from Slic3r was run on the machine. Then, the trajectory generated after establishing the spline-based toolpath and optimizing the feedrate was run. The comparison of the tracking error between the reference trajectory and the measured position can be seen in Figure 4.15 for both cases, with the maximum errors observed and traversal time summarized in Table 4.1.

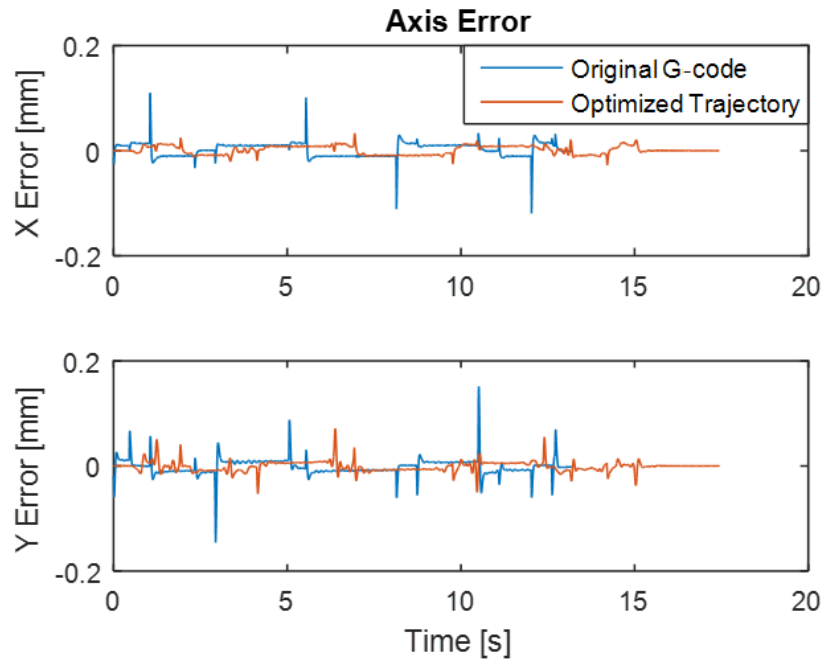


Figure 4.15: Comparison of tracking error in X and Y for the original straight-line G-code path to spline and feedrate optimized path

Table 4.1: Comparison between original straight-line G-code path to spline and feedrate optimized path

	Maximum Error X-axis [mm]	Maximum Error Y-axis [mm]	Traversal Time [s]
Straight-line G-code	0.119	0.150	13.21
Splined and Feedrate Optimized	0.034	0.071	17.43
Percent Change	-72%	-53%	+32%

It can be seen that the error was significantly reduced by using the techniques outlined in this chapter – error reduced in the y-axis by more than 50%, and error reduced in the x-axis by more than 70%. One interesting caveat to note is in traversal time: the optimized trajectory took slightly longer to complete. However, the 30% increase in time is much less than the percent decrease in error, and so this trade-off seems justified.

The PWM-based synchronized dispensing can be validated by comparing the layer from Figure 4.9 extruded when the dispensing is constant, to when PWM is enabled for synchronized dispensing. The results are pictured in Figure 4.16.



Figure 4.16: Evaluation of the effect of the PWM-based synchronized dispensing: on the left is constant dispensing, and on the right is when synchronized dispensing is used.

It is obvious in sharp corners, where the machine slows down, there is extra material dispensed during constant dispensing, causing these corners to be wider than intended. Meanwhile, when the synchronized dispensing is used, the width looks to be even throughout the whole layer, even at the sharp corners, showing the effectiveness of this technique in avoiding inconsistency in width and height.

Chapter 5: Evaluation of Experimentally Manufactured Parts

By applying the developed ink, process models, and trajectory generation techniques described in previous chapters, alginate parts can be manufactured by DBAM. This chapter details simple cylindrical parts that were made to evaluate the fully developed process. The commanded shape, seen in Figure 5.1, was produced at three different porosities, and observations were taken on the final shape, including dimensional and mechanical tests. Section 5.1 outlines the parts to be made, and relevant input parameters and settings used. Section 5.2 outlines observation of the finally manufactured parts, including dimensional measurements. Section 5.3 outlines the results of mechanical testing on these parts, and makes relevant comparisons to literature.

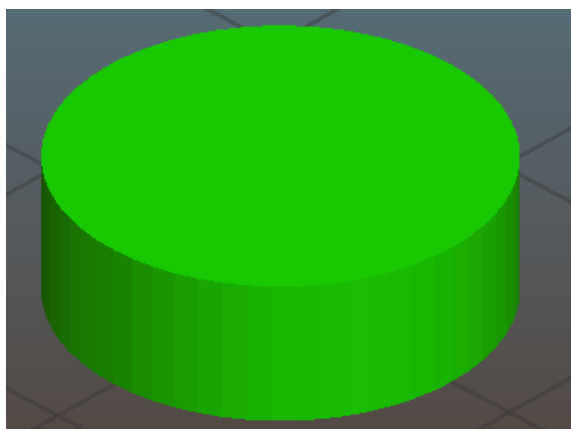


Figure 5.1: Simple cylinder shape to be manufactured to evaluate the DBAM process.

5.1 Input Parameters and Settings Used

The parts were manufactured using the machine that was summarized in Section 4.2.5, integrated with the dispenser presented in Section 4.1.3 and the UV lamp presented in Section 3.2.2.

The commanded shape for the manufacturing parts were simple cylinders of diameter 15mm, and height 5mm. The three cylinders produced were labelled (a), (b) and (c), designed to be 40%, 60% and 80% fill density respectively. The different porosities are accomplished by changing the infill percentage in the Slic3r settings, leading to the layer output from Slic3r seen in Figure 5.2. The resulting commanded final shapes of the parts, as previewed by Slic3r, can be seen in Figure 5.3. A summary of the input parameters used for each manufactured part is seen in Table 5.1.

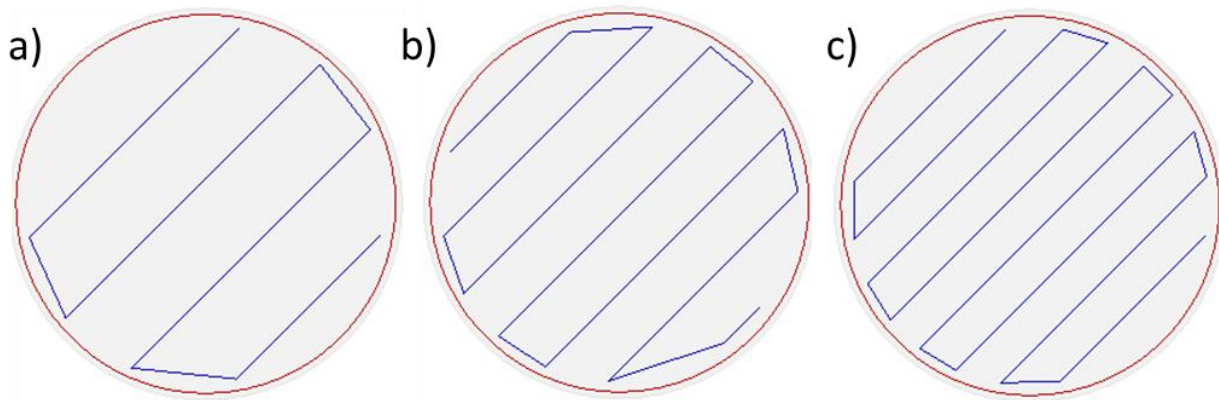


Figure 5.2: Sample layer generated by Slic3r for parts: (a) 40%, (b) 60%, and (c) 80% dense.

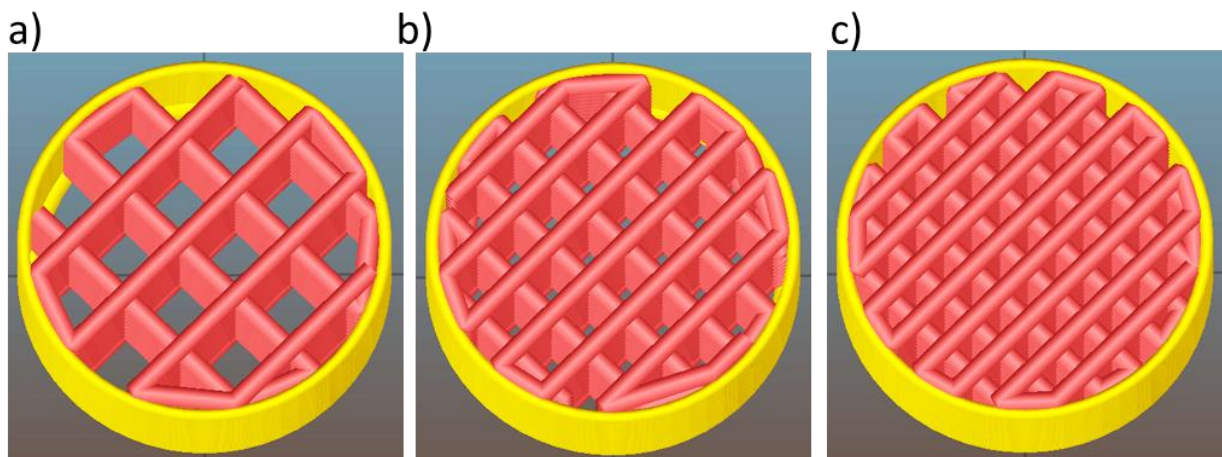


Figure 5.3: Preview of the full shapes in Slic3r: (a) 40%, (b) 60%, and (c) 80% dense.

Table 5.1: Summary of Input parameters used for part manufacturing

Category	Parameter	Part (a)	Part (b)	Part (c)
Part specifications	Part diameter	15 mm		
	Part height	5 mm		
	Part porosity	40%	60%	80%
Ink Components	Concentration of Alginate	8% w-v		
	Concentration of Calcium Carbonate	60 mM		
	Concentration of PAG	120 mM		
Dispense Parameters	Pressure	60 psi		
	Needle Diameter	27 GA (0.21 mm)		
	Needle Length	12.54 mm		
UV exposure parameters	UV lamp intensity	35%		
	Exposure time	90s		
Slic3r Parameters	Layer Height	0.25 mm		

5.2 Observations of Manufactured Part

The three parts in the middle of manufacturing after two layers is pictured in Figure 5.4. The three parts that were finally produced are pictured in Figure 5.5.

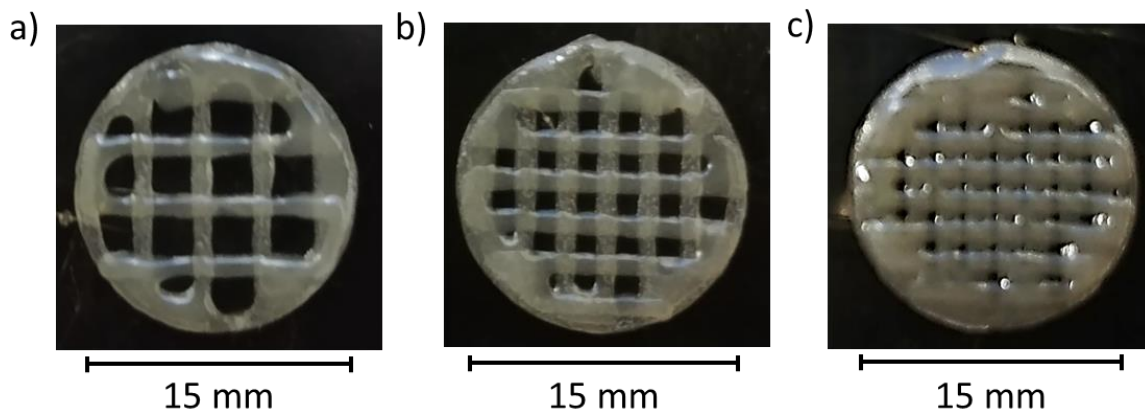


Figure 5.4: Pictures of part after two layers of manufacturing.

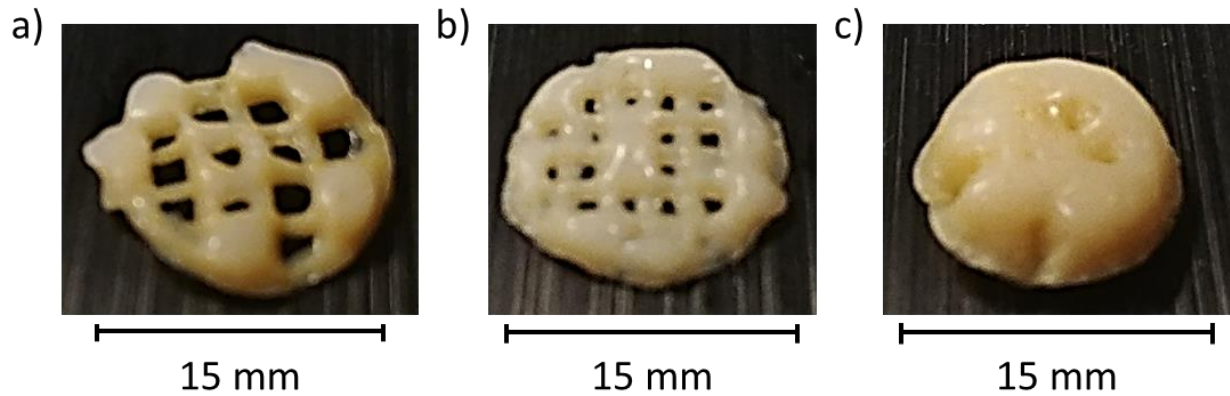


Figure 5.5: Pictures of final manufactured and post-processed parts after 20 layers.

The final parts were solid, showing proper gelation of the liquid alginate ink from which it was made. The part was built up vertically, but there was no evidence of delamination, indicating that the mid-layer gelation was successful in its partial gelation. The final part is circular like the cylinder that was commanded, and the cross-hatching infill is clear, indicating the machine was able to follow and dispense in the commanded shape.

However, the final parts do not exactly represent the cylinder that was commanded. It is noted especially that the width and height is uneven: some sections are much thicker than expected, while some other sections are thinner than expected. In addition, some of the expected spaces between the hatch patterns have been filled in. These unexpected inaccuracies were likely caused by an unexpected flow of the ink after it has been dispensed, distorting the original shape. This flow has been proven to be non-negligible, and has not been modelled. In order to get more accurate shapes without these flowing errors, the ink flow must be mitigated, or modelled and compensated for. In addition, it can be seen that the error propagate through the layers. In the

two layer shape seen in Figure 5.4, not much error is seen. However, little errors are magnified as more layers are applied, causing the larger errors seen in Figure 5.5.

The diameter and height of the manufactured parts are measured, as summarized in Table 5.2

Table 5.2: Summary of diameter and height measure for manufactured parts

	Commanded	Part (a)	Part (b)	Part (c)
Diameter [mm]	15	14.21	13.91	13.01
Height [mm]	5	2.62	2.73	3.21

The measured diameters were smaller than the specified 15mm. However, during the manufacturing process, the machine always dispensed a circle of diameter of 15mm. The diameter discrepancy must occur have occurred after the dispensing, during the post-processing step in calcium chloride solution. Interestingly, this shrinkage seems to be more pronounced when the more dense part (c), corresponding to more alginate in the middle of the shape that would have been crosslinked with the calcium chloride solution. In addition part (c) experienced some swelling, where the middle of the shape became thicker than the outside, likely due to greater shrinkage happening on the outside which is more easily exposed to the calcium chloride solution. Modelling and compensation of the shrinkage due to the calcium chloride solution may be a way to solve the errors noticed here.

The measured heights were much smaller than the specified 5mm. While the post-processing shrinkage previously identified contributes to the error, there are other factors that also result in

this discrepancy. Water loss during the UV exposure, likely leads to a non-negligible loss in the height for a given layer. In addition, height can be lost due to slight collapsing of the partially crosslinked part between layers. Interestingly, the height is larger for the denser parts, likely because the more porous parts have more empty volume in the middle to collapse into. Compensation for the loss of height, perhaps by building higher than commanded, could be used to correct for the error in height. The increased height for the densest part can also be due to the swelling that occurred.

5.3 Evaluation of Mechanical Properties

The three manufactured parts were tested under compression using the Biomomentum Mechanical Tester Mach-1. Uniaxial compression force was loaded at a displacement rate of 0.05 mm/s for a total of 1 mm of displacement in the part. An important parameter for bone scaffolds is compressive stiffness, and that is what was measured, as seen in Table 5.3.

Table 5.3: Measured compressive stiffness of manufactured parts.

	Compressive Stiffness [kPa]
Part (a)	341.2
Part (b)	659.6
Part (c)	726.0

The results further emphasize the success of the process to create solid, stiff parts. As would be expected, an increase in the part density resulted in an increase in compressive stiffness, as there is more material in the shape to resist the compressive force from the testing machine.

To put these measure compressive stiffnesses in context, they can be compared to similar results reported in literature. In Table 5.4 is summarized compressive stiffness for alginate hydrogel from literature, as tested on disks made from different alginate solutions, made using more conventional manufacturing techniques.

Table 5.4: Report Compressive Stiffness of Alginate hydrogel from literature

Author	Alginate Solution used	Compressive Stiffness [kPa]
Jang et al. [27]	2% w-v	70
Stevens et al. [28]	2% w-v	155
	3% w-v	306
	4% w-v	471

As seen in Table 5.4, Stevens et al. prove that higher alginate concentration in solution results in a stiffer part. Taking into account that the relatively high 8% alginate concentration, as well as the porosity of the manufactured parts compared to solid disks, the measured compressive moduli are very close to those represented from the cited literature, indicating that the dispensing based additive manufacturing (DBAM) process outlined in this thesis can produce alginate hydrogel parts of comparable compressive stiffness to other manufacturing processes.

Chapter 6: Conclusion

In this thesis, a method was proposed to manufacture bone scaffolds from alginate using dispensing based additive manufacturing. DBAM process has the advantage of versatility, and uses the biocompatibility and availability of alginate to create bone scaffolds as a treatment for long bone defects. The thesis introduces novel UV activated alginate gelation to convert the liquid ink to a 3D shape after it has been dispensed from the syringe.

An ink consisting of sodium alginate, calcium carbonate and a photoacid generator has been developed which allows for the alginate to gel upon exposure to UV light. For the dispensing step, a model was presented which uses dispenser pressure, needle length and needle diameter as inputs to determine the height and width of a dispensed line. For the mid-layer gelation step, a model was presented which uses UV lamp intensity, exposure time and layer thickness as inputs to determine the mechanical properties of a partially gelled layer. Advanced trajectory generation techniques have been adapted alongside a commercial software called Slic3r to develop a method for converting 3D designed shapes to time-based trajectories for machine movement that would minimize error and traversal time.

The proposed technique was experimentally demonstrated by manufacturing sample parts. The properly shaped created parts demonstrate the validity of the dispensing model, as well as the adapted trajectory generation techniques. The final parts are solid, built up and do not experience delamination, validating the specific developed ink composition, and the model of the UV activated gelation, as the correct level of partial gelation is achieved. The compressive stiffness

of parts created by the proposed technique is comparable to compressive stiffness of alginate scaffolds made by other methods, as reported in the literature.

However, the sample parts do not perfectly represent the commanded shapes, likely due to unmodelled phenomena that exist during the DBAM process. There is evidence that the ink flows after being dispensed, distorting the intended shape of the layer. In addition, the post-processing step in calcium chloride solution, has not been modelled, which can result in some unwanted and uneven shrinkage of parts.

6.1 Future Work

While the experimentally manufactured parts are capable of producing strong solid parts, observations of the produced parts indicate there is still room for improvement in the process. Firstly, unexpected flow of the ink after dispensing can be identified, and techniques can be developed to mitigate its negative effects towards part accuracy. In addition, the shrinkage occurring during the post-processing gelation with the calcium chloride solution can be investigated. If the effect of the calcium chloride crosslinking on the final shape of the part can be modelled, the effect can be mitigated, or the commanded trajectory can be modified to compensate for the expected shrinkage, reduce dimensional error, and eliminate other unwanted artifacts like swelling.

While this project uses an ink with just alginate and materials to assist in the gelation of alginate, dispensing based additive manufacturing allows for other additives to be included in the ink. Ceramic particles, bioactive glass or other polymers can be added into the ink in order to

increase the mechanical stiffness of the final part, or make final parts more biocompatible. Also, work can be done to characterize the biocompatibility of parts manufactured using this process, by conducting further biological experiments with cell cultures, in order to test for biological effectiveness.

Bibliography

- [1] S. Verrier *et al.*, “Tissue engineering and regenerative approaches to improving the healing of large bone defects,” *Eur Cell Mater*, vol. 32, pp. 87–110, 19 2016.
- [2] T. Kurien, R. G. Pearson, and B. E. Scammell, “Bone graft substitutes currently available in orthopaedic practice: The evidence for their use,” *Bone Joint J*, vol. 95-B, no. 5, pp. 583–597, May 2013.
- [3] M. M. Stevens, “Biomaterials for bone tissue engineering,” *Materials Today*, vol. 11, no. 5, pp. 18–25, May 2008.
- [4] S. Bose, S. Vahabzadeh, and A. Bandyopadhyay, “Bone tissue engineering using 3D printing,” *Materials Today*, vol. 16, no. 12, pp. 496–504, Dec. 2013.
- [5] B. P. Hung *et al.*, “Three-Dimensional Printing of Bone Extracellular Matrix for Craniofacial Regeneration,” *ACS Biomater. Sci. Eng.*, vol. 2, no. 10, pp. 1806–1816, Oct. 2016.
- [6] Z. Xiong, Y. Yan, S. Wang, R. Zhang, and C. Zhang, “Fabrication of porous scaffolds for bone tissue engineering via low-temperature deposition,” *Scripta Materialia*, vol. 46, no. 11, pp. 771–776, Jun. 2002.
- [7] J. Franco, P. Hunger, M. E. Launey, A. P. Tomsia, and E. Saiz, “Direct write assembly of calcium phosphate scaffolds using a water-based hydrogel,” *Acta Biomaterialia*, vol. 6, no. 1, pp. 218–228, Jan. 2010.
- [8] L. Geng, W. Feng, D. W. Hutmacher, Y. San Wong, H. Tong Loh, and J. Y. H. Fuh, “Direct writing of chitosan scaffolds using a robotic system,” *Rapid Prototyping Journal*, vol. 11, no. 2, pp. 90–97, Apr. 2005.

- [9] M. G. Li, X. Y. Tian, and X. B. Chen, “A brief review of dispensing-based rapid prototyping techniques in tissue scaffold fabrication: role of modeling on scaffold properties prediction,” *Biofabrication*, vol. 1, no. 3, p. 032001, 2009.
- [10] S. Khalil and W. Sun, “Biopolymer deposition for freeform fabrication of hydrogel tissue constructs,” *Materials Science and Engineering: C*, vol. 27, no. 3, pp. 469–478, Apr. 2007.
- [11] K. Y. Lee and D. J. Mooney, “Alginate: properties and biomedical applications,” *Prog Polym Sci*, vol. 37, no. 1, pp. 106–126, Jan. 2012.
- [12] J. Venkatesan, I. Bhatnagar, P. Manivasagan, K.-H. Kang, and S.-K. Kim, “Alginate composites for bone tissue engineering: A review,” *International Journal of Biological Macromolecules*, vol. 72, pp. 269–281, Jan. 2015.
- [13] C. K. Kuo and P. X. Ma, “Maintaining dimensions and mechanical properties of ionically crosslinked alginate hydrogel scaffolds in vitro,” *Journal of Biomedical Materials Research Part A*, vol. 84A, no. 4, pp. 899–907, 2008.
- [14] A. G. Tabriz, M. A. Hermida, N. R. Leslie, and W. Shu, “Three-dimensional bioprinting of complex cell laden alginate hydrogel structures,” *Biofabrication*, vol. 7, no. 4, p. 045012, 2015.
- [15] V. Javvaji, A. G. Baradwaj, G. F. Payne, and S. R. Raghavan, “Light-Activated Ionic Gelation of Common Biopolymers,” *Langmuir*, vol. 27, no. 20, pp. 12591–12596, Oct. 2011.
- [16] A. K. Higham, C. A. Bonino, S. R. Raghavan, and S. A. Khan, “Photo-activated ionic gelation of alginate hydrogel: real-time rheological monitoring of the two-step crosslinking mechanism,” *Soft Matter*, vol. 10, no. 27, pp. 4990–5002, 2014.

- [17] T. M. Valentin *et al.*, “Stereolithographic printing of ionically-crosslinked alginate hydrogels for degradable biomaterials and microfluidics,” *Lab on a Chip*, vol. 17, no. 20, pp. 3474–3488, 2017.
- [18] F. Mainardi and G. Spada, “Creep, Relaxation and Viscosity Properties for Basic Fractional Models in Rheology,” *The European Physical Journal Special Topics*, vol. 193, no. 1, pp. 133–160, Mar. 2011.
- [19] Dey Arindam and Basudhar P. K., “Applicability of Burger Model in Predicting the Response of Viscoelastic Soil Beds,” *GeoFlorida 2010*.
- [20] “IntelliRay | Full-Featured UV Flood Curing System.” [Online]. Available: <https://www.uvitron.com/products/floods/intelliray.php>. [Accessed: 27-Mar-2019].
- [21] C. Hu, Y. Tang, X. Song, Z. Liu, and B. Zhang, “Ultrafast Photodissociation Dynamics of Highly Excited Iodobenzene on the C Band,” *J. Phys. Chem. A*, vol. 120, no. 51, pp. 10088–10095, Dec. 2016.
- [22] Z. Guo, R. Ma, and G. Li, “Degradation of phenol by nanomaterial TiO₂ in wastewater,” *Chemical Engineering Journal*, vol. 119, no. 1, pp. 55–59, Jun. 2006.
- [23] “Techcon Systems TS 350/355 Precision Dispensers User Guide.” OK International.
- [24] B. Sencer, Y. Altintas, and E. Croft, “Feed optimization for five-axis CNC machine tools with drive constraints,” *International Journal of Machine Tools and Manufacture*, vol. 48, no. 7, pp. 733–745, Jun. 2008.
- [25] A. Yuen, K. Zhang, and Y. Altintas, “Smooth trajectory generation for five-axis machine tools,” *International Journal of Machine Tools and Manufacture*, vol. 71, pp. 11–19, Aug. 2013.

- [26] “Slic3r - Open source 3D printing toolbox.” [Online]. Available: <https://slic3r.org/>.
[Accessed: 03-Mar-2019].
- [27] J. Jang, J. Lee, Y.-J. Seol, Y. H. Jeong, and D.-W. Cho, “Improving mechanical properties of alginate hydrogel by reinforcement with ethanol treated polycaprolactone nanofibers,” *Composites Part B: Engineering*, vol. 45, no. 1, pp. 1216–1221, Feb. 2013.
- [28] M. M. Stevens, H. F. Qanadilo, R. Langer, and V. Prasad Shastri, “A rapid-curing alginate gel system: utility in periosteum-derived cartilage tissue engineering,” *Biomaterials*, vol. 25, no. 5, pp. 887–894, Feb. 2004.